Politecnico di Torino

Corso di Laurea Magistrale in Ingegneria Aerospaziale
A.A. 2024/2025
Tesi di Laurea Magistrale

Experimental Characterization and Modeling of Nonlinear Effects in Electromechanical Actuators for Prognostic Capabilities

Relatore:
Matteo Davide Lorenzo Dalla Vedova

Candidato:
Antonio Leone Pinello

Correlatori:
Paolo Maggiore
Matteo Bertone

Abstract

With the advent of modern power electronics and the advancement of aircraft system technologies—along with the need for reduced operating costs and emissions—the new concept of More Electric Aircraft (MEA) has gained traction in the aerospace industry. This paradigm aims to replace all non-propulsive systems onboard the aircraft with electrically powered alternatives. In this context, both primary and secondary flight control systems must meet the demanding performance and reliability standards traditionally achieved by high-power hydraulic actuators, adopting instead a new approach based on Electromechanical Actuators (EMAs).

The work presented in this thesis aims to implement design modifications on an experimental EMA test bench, enabling it to accurately reproduce various operating conditions typical of these servomechanisms. Representative phenomena such as gear backlash and actuation friction are introduced into the test setup in a controlled manner, by means of the linear displacement of two precision micro-movers. In addition, mutual validation with a simulation model was considered essential for gaining insight into the behavior of such systems.

The test bench assembled can be broadly divided into two functional sections. The first is responsible for generating high-torque, low-speed power, using a conventional synchronous electric motor-reduction gearbox assembly. An incremental encoder is connected to this assembly via a gear interface that allows adjustable backlash and closes the position feedback control loop. The second section is dedicated to generating a friction torque on the actuation line through a brake-disc mechanism. This allows for the regulation of the distance between the brake pad and the disc, while the torque produced is measured via a load-cell lever system.

An experimental campaign was conducted to accurately measure and map the key monitored variables and compare them with the outputs of the system's simulation model. The variables analyzed were sampled during system operation, and the observed trends confirmed both the non-linear nature of these phenomena and a good degree of accuracy of the model under nominal conditions. The updated test bench–model framework lays the groundwork for future model-based prognostic capabilities, potentially enhancing both the understanding and reliability of modern EMA systems.

Table of Contents

List of Tables

List of Figures

Chapter 1

Introduction

1.1 Outline of the work

This thesis is organised into seven chapters, each addressing a specific aspect of the study and contributing to the overall understanding of the experimental and modelling work carried out.

Chapter 1 introduces the context of More Electric Aircraft technologies and the motivation behind the study, outlining the challenges associated with modelling and characterising electromechanical actuation systems.

Chapter 2 describes in detail the architecture of the experimental EMA test bench, highlighting the modifications implemented to enhance its capability to reproduce nonlinear phenomena such as dry friction and gear backlash.

Chapter 3 presents the mathematical and simulation model developed in Simulink, providing a comprehensive overview of the electromechanical, control, and transmission subsystems, and the modelling strategies adopted.

Chapter 4 discusses the experimental methodology and the data-acquisition framework designed to collect and process measurements from the test bench, including the mapping procedures for friction torque and gear backlash.

Chapter 5 reports the experimental campaign carried out on the modified test bench, describing the test matrix, the measured variables, and the observed behaviours under different operating conditions.

Chapter 6 provides a detailed comparison between experimental results and model predictions, including error analysis, spectral investigations, and an assessment of computational performance.

Finally, **Chapter 7** summarises the main findings of the thesis, draws conclusions on the effectiveness of the proposed approach, and outlines potential directions for future developments.

1.2 More Electric Aircraft

Traditionally designed aircrafts leverage hydraulic and pneumatic systems to provide power to secondary utilities, extracting it from the aircraft main engines in different ways.
In particular, hydraulic systems are conventionally tasked with actuating flight controls and operating the landing gear.
This type of actuation, despite being significantly robust and reliable, presents some intrinsic drawbacks, such as low efficiency, challenges in detecting leaks within pneumatic systems, the need for multiple gearboxes in mechanical configurations, the presence of heavy and complex piping, and the inherent risks associated with fluid leaks in hydraulic systems.[1].
These factors, combined with advancements in electrical technology and the growing need to optimize energy consumption, have driven the industry toward a design paradigm that favors the use of electrical power for the extraction and distribution of non-propulsive power. This trend is defined as More Electric Aircraft (MEA).[2].

As stated in the introduction, the MEA design philosophy aims to employ electrical power in secondary systems, and is based around the concept of generating it from the main engines.
Mechanical energy with controllable speed and torque represents a highly valuable form of energy required by various aerospace systems. However, its distribution and transport pose significant challenges. Converting this energy into electrical form enables efficient delivery to the required locations, with minimal losses, reduced weight, and reasonable cost. [3]
Compared to the traditional hydraulic architecture, where mechanical power from the engine is extracted to drive the pumps of the various hydraulic circuits, the MEA systems present the major advantage that the electrical power required by systems already relying on it—such as avionics, entertainment, and others—has grown so significantly that the additional demand from actuation systems has become comparable. As a result, since large generators are already installed, it becomes convenient to use them for all purposes. Moreover, distributing electrical power through cables, rather than routing high-pressure hydraulic lines, allows for more flexible and safer configurations. Finally, MEA systems present the major advantage of increasing the thermodynamic efficiency of the engines. This results in a reduction in fuel consumption up to 9%, and in a decrease of 1% in terms of take-off weight. [1]

Furthermore, relying on a single energy source enables greater integration of aircraft subsystems and leads to a significant reduction in both maintenance operations and costs, due to the substantial decrease in the number of components.

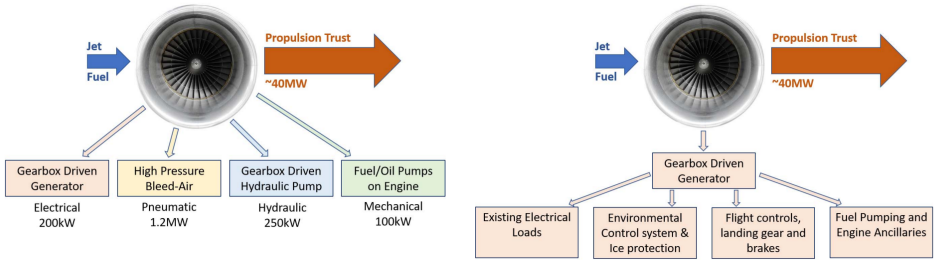

Figure 1.1: Subsystem comparison between conventional (left) and MEA (right) aircraft

Still, as of today, the use of Electromechanical Actuators (EMAs) is largely restricted to secondary flight controls—such as airbrakes, spoilers, and high-lift devices—on large aircraft (such as the Boeing 787 and the Airbus A380). They are employed as primary flight control actuators mainly in small UAVs or, more broadly, in applications where the failure of the actuation system is not mission-critical and does not pose a risk to human life or involve the loss of high-value assets. This limitation is partly due to the fact that EMAs remain a relatively new technology in the aerospace sector: their combined fault modes are not yet fully understood, and established prognostic methodologies are generally lacking.[4].

1.3 Prognostics

Prognosis is the ability to accurately and precisely predict the remaining useful life (RUL) of a failing component or subsystem, enabling timely isolation or replacement.[5]
Modern Prognostics and Health Management (PHM) begins with Fault Detection and Identification (FDI), a phase in which early signs of developing faults are recognized by analyzing the system's response. The information obtained during this stage is then used to estimate the RUL.
FDI strategies are generally divided into two main categories: model-based and data-driven techniques, which differ fundamentally in their approaches. [4]

- **Model-based FDI** relies on comparing the actual behavior of the system with the output of a simulation model developed for health monitoring purposes.
- **Data-driven FDI** methods replace detailed physical knowledge of the system

with large datasets of recorded system outputs. These datasets are then processed using machine learning algorithms to estimate the health status of the real system.

Model-based methods utilize residuals as diagnostic features, where residuals are defined as the outcomes of consistency checks between measured sensor data from the actual system and the corresponding outputs generated by a mathematical model. The underlying assumption is that residuals remain small in the presence of normal disturbances, noise, and modeling inaccuracies, but become significantly larger when faults occur.
This approach is particularly suitable when accurate mathematical models can be derived from first principles. One of its main advantages is the ability to embed physical understanding of the system into the monitoring process.
Moreover, as the understanding of system degradation mechanisms improves, the model can be refined to enhance its accuracy and to capture subtle performance degradations. As a result, model-based approaches can offer superior performance compared to data-driven methods in many applications.[6]

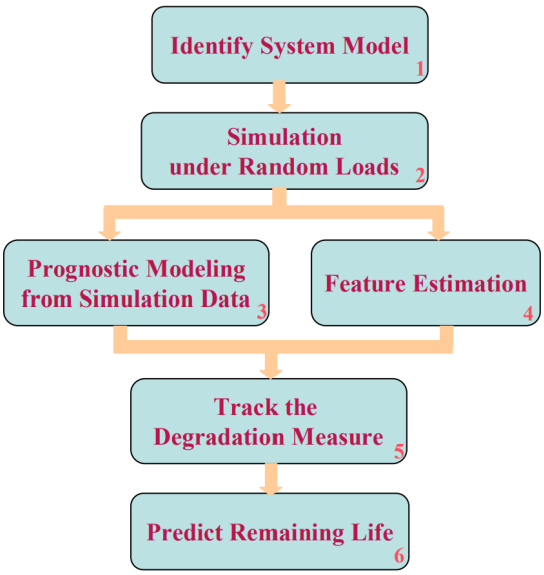

Figure 1.2: Model-based prognostic process

1.4 Electromechanical actuator (EMA)

A central element in the electrification of aircraft actuation systems is the electromechanical actuator. This subsystem enables the conversion of electrical power into mechanical power used for controlling primary or secondary aerodynamic surfaces, deploying landing gear, and other actuation purposes. The general architecture of such systems is composed of:

- **Electric Motor (EM)**, such as a three-phase Brushless DC Motor (BLDC) or, more commonly, a Permanent Magnet Synchronous Motor (PMSM).
- **Power Drive Electronics**, which provide the appropriate power commands to operate the electric motor, according to the type of motor selected and the feedback signal received from the EM.
- **Actuator Control Electronics**, used in servoactuators, which implement the control logic to regulate the actuator's position (or velocity) as commanded by the pilot/Flight Control Computer.
- **Reduction Drive (Gearbox)**, used to convert the high-speed, low-torque output of the EM into the low-speed, high-torque input required by the actuation system. In fact, since the size and weight of an EM scale with the torque it generates, aerospace systems typically prefer to produce a high-speed, low-torque output and then convert it to the required high torque using a gearbox (usually high-efficiency planetary gearboxes).

In the particular case of linear actuators, an additional component is required, responsible for converting the rotary motion delivered by the EM into the linear motion used in actuation.
The main solution employed is the screw-nut coupling. Since aerospace systems demand a high level of robustness and reliability, sliding screw solutions—which are prone to backlash and instability due to friction and wear—are replaced with more reliable recirculating ball (or roller, if the required ball diameter is too small) systems.[3] In Figure 1.4 the logic scheme of a generic EMA (Electromechanical

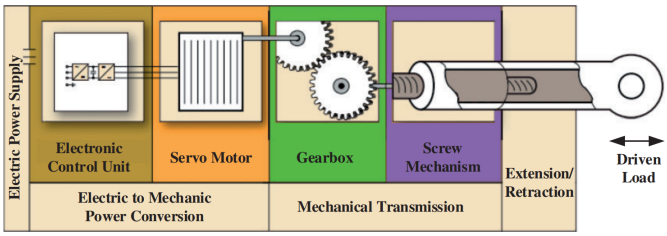

Figure 1.3: Electromechanical Actuator – General Layout

Actuator) is shown. The bold red arrows represent the high-power line, the thin red arrows the low-power line, and the dashed arrows represent the signal lines.
The pilot or FCS issues a command that is sent as an input to the Actuator Control Electronics, which also receives the measured position from the end user.
The control logic then computes a signal that is sent to the Power Drive Electronics, which—through the inverter subsystem, properly fed with rotor position feedback from the EM encoder—powers the Electric Motor accordingly.
The torque generated by the EM is transmitted to the gearbox, where it is converted, and then delivered to the final user.
The position of the final user is sent back to the Actuator Control Electronics, closing the outer feedback loop and thus enabling control.

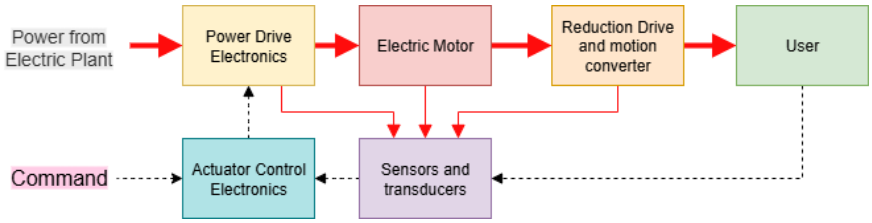

Figure 1.4: Electromechanical Actuator – Logical Scheme

1.4.1 Permanent Magnet Synchronous Motor

Given the scope of this work, a brief description of the Permanent Magnet Synchronous Motor (PMSM) is provided in the following section.

Synchronous motors require an AC supply for the stator windings and a DC supply for the rotor windings. The rotational speed of the motor is determined by the frequency of the AC supply and the number of poles in the motor. At synchronous speed—which is constant—the rotor rotates in synchrony with the stator's revolving magnetic field.
One particular type of synchronous motor is the Permanent Magnet Synchronous Motor (PMSM). The PMSM features a conventional three-phase winding in the stator and permanent magnets mounted on the rotor. In this configuration, the role of the field windings in traditional synchronous machines is fulfilled by the permanent magnets. Unlike conventional synchronous motors, which require both AC and DC supplies, the PMSM operates solely with an AC supply. This elimination of the DC excitation system is one of the key advantages of the PMSM, resulting in improved reliability and simplified system architecture.
The synchronous speed ω_s of the motor is determined by the frequency f_s of the

stator input supply and the number of pole pairs p, according to the relationship:

$$\omega_s = 2\pi \frac{f_s}{p} \qquad \text{rad/s}$$

In a three-phase synchronous machine, the stator contains a distributed sinusoidal winding, while the rotor includes the same number of pole pairs as the stator, excited either by permanent magnets or a separate DC source.[7]

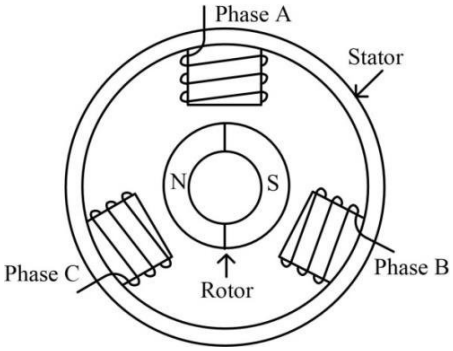

Figure 1.5: Basic structure of a Synchronous Motor

When a three-phase AC supply is applied to the stator, a rotating magnetic field is produced, which revolves at the synchronous speed.
Several control strategies can be employed for Permanent Magnet Synchronous Motors (PMSMs), including scalar control, vector control, and field-oriented control (FOC). Scalar control is a basic technique that provides satisfactory speed regulation but offers poor torque performance. In contrast, more advanced methods such as vector control and field-oriented control allow for precise control of both speed and torque. Field-oriented control operates by manipulating the orientation of the motor's magnetic field, while vector control is based on the decoupling of the motor's torque and flux components to achieve dynamic performance comparable to that of a DC motor.
PMSMs offer several advantages over other types of electric motors. Thanks to their high power density, they can deliver substantial power output while remaining compact and lightweight. Their high efficiency allows for the conversion of a large portion of the electrical input into mechanical energy, making them well-suited for energy-sensitive applications. Moreover, PMSMs require minimal maintenance, as they lack brushes and commutators. Their use of permanent magnets in the rotor also contributes to a long operational lifespan, as these components are highly resistant to wear and degradation.[8].

1.4.2 Failure Modes, Effects, and Criticality Analysis

A Failure Modes, Effects, and Criticality Analysis (FMECA) conducted on EMA actuators by NASA has provided insight into the most relevant failure modes and their likelihood of occurrence. [9]
The key findings are presented in the following table:

Item / Component	**Failure Rate (HR^{-1})**	**Failure Mode Mechanism**
Bearings	1.78E-05	Increased friction due to: - bearing wear - galling
Position Sensor	1.70E-05	Loss/incorrect feedback signal from resolver: - Turn-to-turn short - Turn-to-ground short - Open circuit
Brushless DC Motor	1.03E-05	Breakdown of stator assembly insulation due to: - Turn-to-turn short - Phase-to-phase short - Turn-to-ground short - Open circuit
Power Connector	6.64E-07	Electrical open due to: - Open pin - Open leadwire

Table 1.1: Failure Modes and Rates of EMA actuators

1.5 Friction in actuation mechanisms

All real-world engineering applications involving components with relative motion are characterized by some form of friction. In particular, flight controls—being position servomechanisms that demand high accuracy—require a deep understanding of friction phenomena.
While an initial empirical understanding of friction dates back to the 15th century—Leonardo da Vinci first described it as a force opposing motion and proportional to the applied load—a rigorous and accurate modeling of the phenomenon is a subject of modern research.
In fact, friction is a non-linear phenomenon and, as such, requires the use of suitably complex modeling techniques.
Moreover, the control of systems affected by friction demands special attention, as effects such as hysteresis, frictional memory, pre-sliding displacement, and stick-slip can compromise standard control strategies.[10].

One of the most challenging aspects of friction modeling lies in accurately representing behavior around zero velocity. From a physical perspective (according to Coulomb's model), the friction force does not have a unique value at $v = 0$; instead, it equals the external load if the latter does not exceed the static friction threshold, or it transitions to the dynamic friction value otherwise. Therefore, a comprehensive friction model must be capable of correctly handling the following four kinematic conditions [11]:

1. A mechanical element initially at rest that must remain stationary
2. A mechanical element initially at rest that must start moving
3. A mechanical element already in motion that must continue moving
4. A mechanical element already in motion that must come to a stop

In order to meet these requirements, one of the most effective approaches to friction modeling is the use of event-based algorithms (like the Borello Friction Model, which will be discussed later in this work): if, at zero velocity, the applied force is smaller than the static friction force, the friction force equals the applied force and no motion occurs.
If, instead, the applied force exceeds this threshold, the friction force transitions to the Coulomb friction force or, depending on the model, to the viscous friction force.

1.5.1 Stick-slip phenomenon

The stick-slip phenomenon typically occurs at low actuation speeds and cannot be adequately explained by a simple Coulomb friction model.
To understand this particular behavior, a simple example system is introduced. A mass M is constrained to a fixed support on the left by means of a translational spring and rests on a frictional surface, sliding at a constant speed v [11].

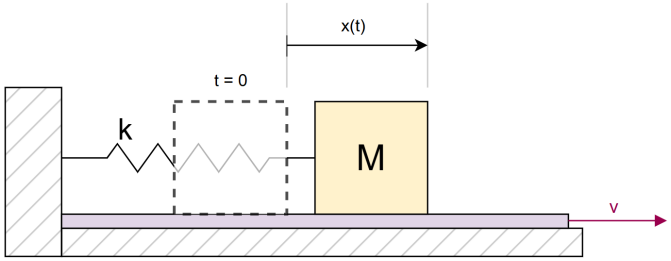

Figure 1.6: Example system representation

When the surface begins to move at $t = 0$, the equation of motion for the mass M is:

$$M\ddot{x} = F_s - F_{el}$$

That is, until the elastic force $F_{el}(t) = kx(t)$ equals the static friction force, the mass moves with the sliding surface (stick phase), and therefore moves at constant speed v after a first transient phase.
At time $t = t_1$ the elastic force equals the static friction force:

$$F_{el}(t_1) = kx(t_1) = \mu_s N = \mu_s Mg \quad \Rightarrow \quad x(t_1) = \frac{\mu_s N}{k}$$

At $t = t_1$, the mass detaches from the surface, and the friction force shifts from the static regime $F_s = \mu_s N$ to the dynamic one $F_d = \mu_d N$ (characterized by a lower magnitude) thus initiating the slip phase.
The equation of motion during the slip phase is therefore given by:

$$M\ddot{x} = \mu_d N - kx(t)$$

With initial conditions:

$$\begin{cases} x(t_1) = \frac{\mu_s N}{k} \\ \dot{x}(t_1) = v \end{cases}$$

This second-order differential equation can be solved under the hypothesis of small values of v (coherent with the phenomenon analyzed in this section), resulting in

the following equation for the state $x(t)$ during the slip phase:

$$x(t) = \frac{\mu_d N}{k} + \frac{(\mu_s - \mu_d)N}{k} \cos\left(\sqrt{\frac{k}{M}} \cdot t\right)$$

Representing a harmonic behavior, characterized by an amplitude $A = \frac{(\mu_s - \mu_d)N}{k}$, a period $T = 2\pi\sqrt{\frac{M}{k}}$ and an initial offset $x(t_1)$.
The slip phase ends when the mass M reaches zero relative velocity w.r.t the sliding surface, initiating a new stick phase. The system then continues to alternate between these two phases [11].

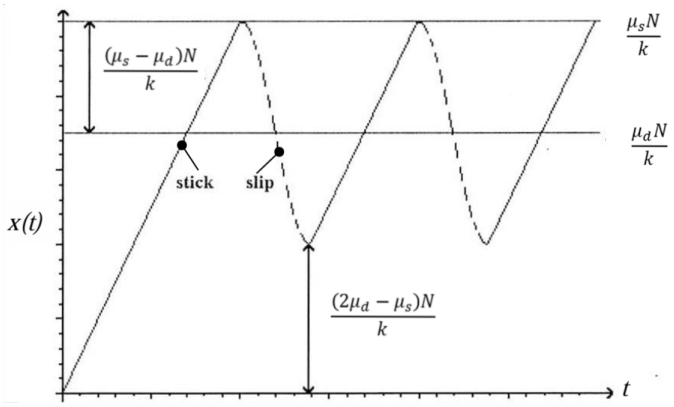

Figure 1.7: Stick-slip behavior of the example system

The first aspect to highlight is that, for a system with fixed k and M, the oscillatory behavior depends solely on the difference between the static and dynamic friction coefficients.
Secondly, it is of interest to investigate how the system's behavior changes as the ratio v/ω varies. As the velocity v increases, the duration of the stick phase T_{stick} progressively decreases, approaching zero (i.e., pure slipping motion) for relatively high values of v:

$$T_{\text{stick}} = \frac{2(\mu_s - \mu_d)N}{kv} \sim \frac{1}{v}$$

The duration of the slip phase T_{slip} must instead be determined by iteratively solving the following transcendental equation:

$$v(\cos \omega T_{\text{slip}} - 1) - \frac{(\mu_s - \mu_d)N}{k} \omega \sin \omega T_{\text{slip}} = 0$$

The qualitative results for $M = 1\ kg$, $k = 25N/m$, $\mu_s = 1$, $\mu_d = 0.5$ are presented in Figure 1.8. [11]

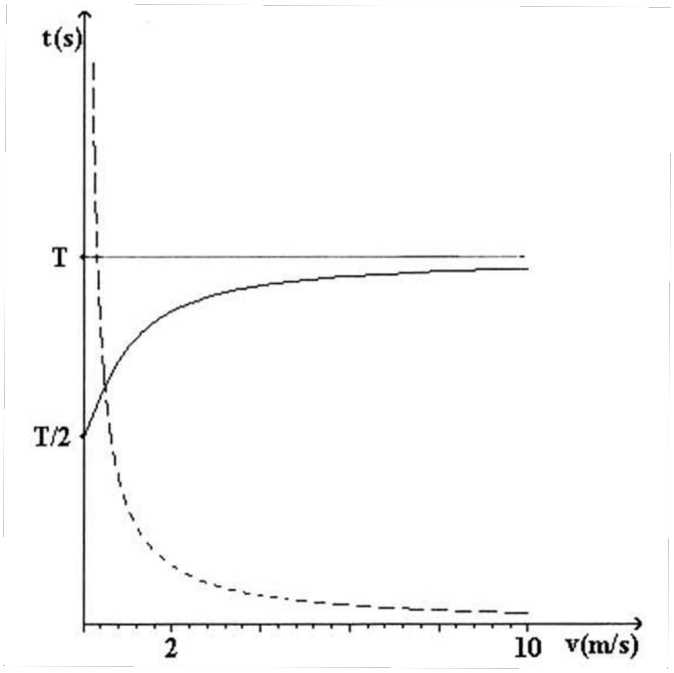

Figure 1.8: T_{stick} (solid line) and T_{slip} (dashed line) as a function of velocity v

Chapter 2

EMA test bench description

In order to thoroughly investigate the prognostic capabilities and to validate the model proposed in Chapter 3, an updated version of an experimental test bench—originally designed by the ASTRA research group at Politecnico di Torino—was set up.
The test bench, depicted in Figure 2.1, can be macroscopically divided into two main modules: an actuation module—responsible for executing and properly controlling position commands—and a braking module—designed to reproduce and test friction conditions affecting the actuation system.

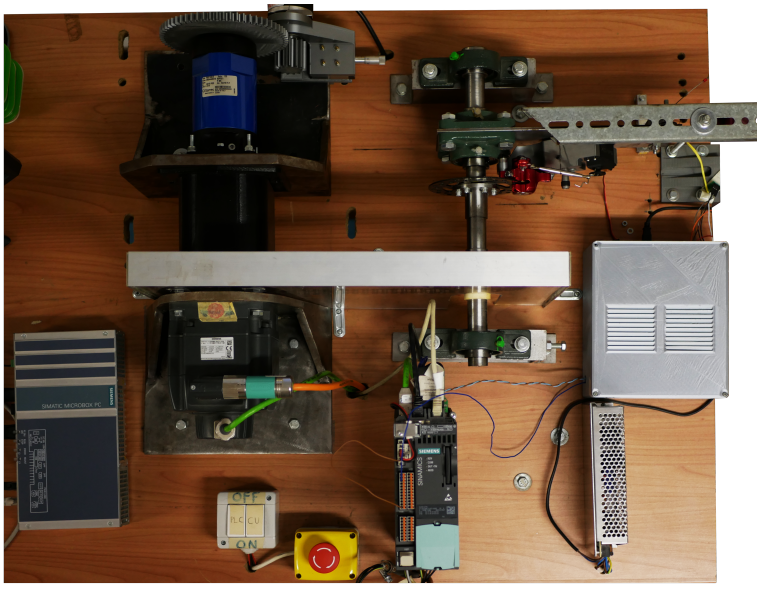

Figure 2.1: EMA test bench

2.1 Actuation module

The actuation module consists of the electric motor, the power supply and control subsystem—comprising the PLC, control unit (CU), inverter, and voltage converter—and the transmission subsystem, which includes the gearbox and its encoder.

2.1.1 Electric Motor

The electric motor employed is a Simotics S-1FK7060-2AC71-1CG0, a permanent magnet synchronous motor (PMSM) manufactured by Siemens and included in the Sinamics S120 AC/AC Trainer Package, along with the PLC, Control Unit (CU), and inverter.
The motor integrates a dedicated encoder, which is used by the Control Unit to supply the appropriate voltage to each of the motor phases.
It is mounted on the test bench using a custom-designed steel support, which ensures proper alignment between the motor's output shaft and the gearbox for angular speed reduction. The connection between the motor and the gearbox is achieved through a flexible coupling joint.
In Table 2.1, the motor datasheet is reported. It is worth noting that the speed limit imposed by the inverter's current-switching capabilities is significantly lower than the mechanical speed limit, which is constrained by centrifugal forces and wear.

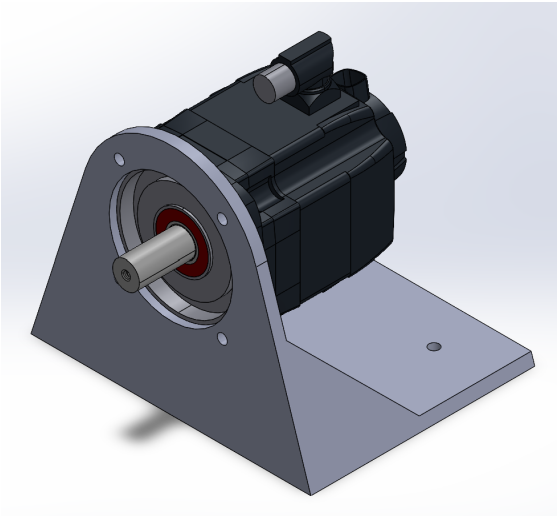

Figure 2.2: Electric Motor and steel support

Mechanical data	
Motor Type	PMSM
Cooling	Natural cooling
Moment of inertia	7.700 kgcm^2
Shaft torsional stiffness	40,500 Nm/rad
Net weight of the motor	7.1 kg
Engineering data	
Rated speed (100 K)	2,000 rpm
Number of poles	8
Rated torque (100 K)	5.3 Nm
Rated current	3.0 A
Efficiency	90.0 %
Physical constants	
Torque constant	1.91 Nm/A
Voltage constant at 20°C	121.0 V/1000·min^{-1}
Winding resistance at 20°C	2.75 Ω
Rotating field inductance	30.5 mH
Electrical time constant	11.10 ms
Mechanical time constant	1.75 ms
Thermal time constant	30 min
Optimum operating point	
Optimum speed	2,000 rpm
Optimum power	1.1 kW
Limiting data	
Max. permissible speed (mech.)	7,200 rpm
Max. permissible speed (inverter)	4,750 rpm
Maximum torque	18.0 Nm
Maximum current	10.7 A

Table 2.1: Electric Motor datasheet

2.1.2 SIMATIC Microbox PC

The Simatic Microbox PC serves as the main processing and control unit of the actuation system, functioning as a virtualized PLC.
It is a passively cooled, compact PC running a Windows Embedded operating system, which hosts the STARTER software. This software is used to configure control commands and to record operating variables such as the gearbox and motor encoder positions, motor speed, and phase currents within the windings.

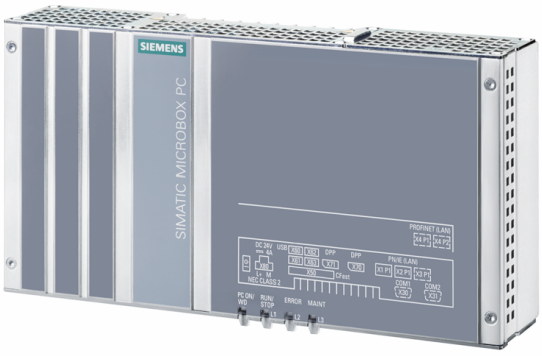

Figure 2.3: Microbox PC

Processor	Intel Core i3-6102E
Memory	16 Gb DDR4 RAM 128 Gb SSD
Operative system	Windows Embedded Standard 7 SP1, 64 bit
Graphic	Integrated HD graphic
Ports	4x USB V3.0 3x Gbit Ethernet 2x Display Port DPP
Power supply	24V DC
Operative temperatures	0°C to 55°C
Dimensions	W: 262 mm; H: 139.7 mm; D: 55.5 mm

Table 2.2: Microbox PC datasheet

2.1.3 Control Unit

The Control Unit (CU) consists of a SINAMICS CU310-2 PN module. It receives motor position feedback from the dedicated encoder and command signals from the PLC, and processes this information to generate the appropriate power signals, thereby controlling the inverter.
The position data is transmitted via a DRIVE-CLiQ cable (a Siemens proprietary communication interface), while the commands from the PLC are received through an Ethernet connection. The CU is directly connected to the inverter through a dedicated interface.

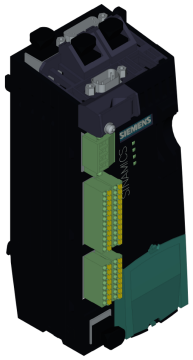

Figure 2.4: SINAMICS CU310

Power supply	24V DC (max 0.8A)
Encoder frequency, max	300 kHz
Number of digital inputs	11
Number of digital I/O	8
Digital signals voltage	-3V to 30V
Digital signals low level	-3V to 5V
Digital signals high level	15V to 30V
Number of analog input	1
Operative temperatures	0°C to 55°C
Dimensions	W: 73 mm; H: 191 mm; Depth: 75 mm

Table 2.3: Control Unit datasheet

2.1.4 Inverter

The purpose of the inverter is to supply power to the motor windings according to the commands issued by the Control Unit (CU). The inverter used is part of a PM240-2 Blocksize Power Module, which is powered by a 380V three-phase supply and therefore requires a dedicated power line.
The Power Module additionally includes a diode rectifier, which converts the three-phase AC supply into DC power to feed the inverter stage..
The product datasheet is reported in Table 2.4.

Input	
Number of phases	3 AC
Line voltage	380V to 480V
Line frequency	47 Hz to 63 Hz
Rated current	2.00 A
Output	
Number of phases	3 AC
Pulse frequency	4 kHz
General specifications	
Power factor	0.85
Efficiency	0.96
Cooling	Internal air cooling
Operative temperatures	-5°C to 40°C
Net weight	1.50 kg
Dimensions	W: 73 mm; H: 196 mm; D: 165 mm

Table 2.4: PM240-2 Blocksize datasheet

2.1.5 Gearbox

As introduced in Section 1.4, EMA systems typically employ gearbox speed reducers to convert the torque from the electric motor's output shaft.
The test bench used in this study was originally equipped with a custom-designed two-stage planetary gearbox, featuring an overall reduction ratio of 1:124 and manufactured using Fused Deposition Modeling (FDM).
Although the original design allowed for high transmission ratios and reduced manufacturing costs, the materials employed introduced notable performance drawbacks.
The main drawbacks were related to the low torsional stiffness of the gearbox shafts and the tendency of the teeth to deform—factors that significantly limit the allowable operating loads, introduce substantial difficulties in the analysis of system backlash, and, more importantly, require a highly complex and computationally demanding mathematical model to achieve the desired high-fidelity characteristics.
Thus, one of the main upgrades to the test bench presented in this work consists of the adoption of an off-the-shelf, industry-grade planetary gearbox. This solution allows for the overall mitigation of the previously described drawbacks of the original design, primarily due to its low internal backlash, which enables a more accurate study of this phenomenon, as will be discussed in greater detail in Section 2.1.6. The adopted model is a Tramec REP100/3C 120 AU19FLT AE19 P05, featuring a reduction ratio of 120 , and it is mounted on a steel support similar to the one used for the electric motor.

Quantity	**Value**
Step number [-]	3
Nominal ratio [-]	120
Moment of inertia (input shaft) [kg cm^2]	0.59
Weight [kg]	4.5
$n_{1_{\text{nom}}}$ [min^{-1}]	5000
$n_{1_{\text{max}}}$ [min^{-1}]	6000
Standard backlash α_{max} [arcmin]	8

Table 2.5: Gearbox datasheet

2.1.6 Encoder

The encoder assembly serves the purpose of closing the position feedback loop at the end of the motor–gearbox assembly, transmitting this information back to the PLC and thereby enabling closed-loop position control. Its placement on the slow shaft ensures that the controlled variable corresponds to the actual output of the transmission, thereby increasing the reliability of the feedback information used by the control logic.

The encoder employed is an Italsensor TSW581HS (a summarized datasheet is provided in table 2.6). Being an optical incremental encoder, it can only provide measurements relative to its initial condition. Therefore, two output signals, A and B, are required to detect both the position and the direction of rotation, using two coded disks with sectors that are out of phase. The direction of rotation is determined by observing which of the two channels leads, while the position is measured by counting the signal fronts from both channels.

In addition, the assembly facilitates the investigation of different backlash conditions at the transmission output. This is made possible by exploiting the linear micro-mover on which the encoder is mounted, which allows controlled variation of the center distance between the encoder gear and the gear located on the gearbox output shaft. In this way, a wide range of backlash values can be experimentally reproduced and analysed under realistic operating conditions.

Figure 2.5b illustrates the coupling between the gearbox and the encoder. The micro-mover (in purple) is free to slide along the supporting guide (in green), thereby modifying the relative distance between the encoder gear (cyan) and the gearbox output-shaft gear (brown). Both gears were manufactured using FDM, allowing rapid iteration of different geometries during the development of the experimental setup.

Resolution	10,000 ppr
Power supply	5 V DC
Output frequency	Up to 300 kHz
Starting torque @ 25°C	0.025 Nm
Moment of inertia	40 g cm^2

Table 2.6: Encoder datasheet

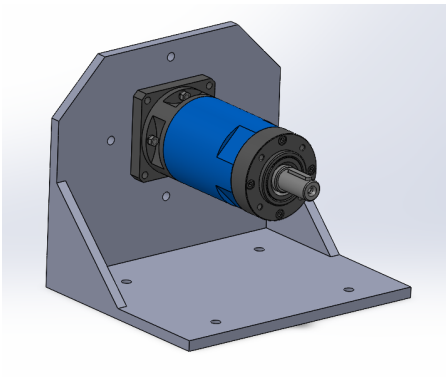

(a) Planetary gearbox and steel support

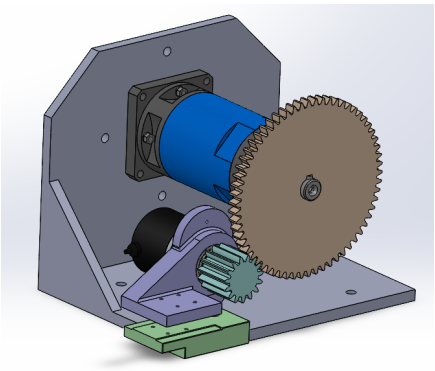

(b) Encoder–Gearbox Coupling

Figure 2.5

Experimental Backlash Adjustment

Backlash in gears represents the clearance, or play, between the mating teeth of two meshing gears. While a small amount of backlash can be desirable—since it prevents gear jamming and provides space for lubrication as well as differential thermal expansion—it is a phenomenon that must be carefully controlled and accurately studied, as it can compromise position control in servomechanisms and, more broadly, degrade overall system performance.
In the test bench described in this section, backlash is regulated for experimental purposes by adjusting the center distance through the use of the micro-mover, as depicted in Figure 2.6a.

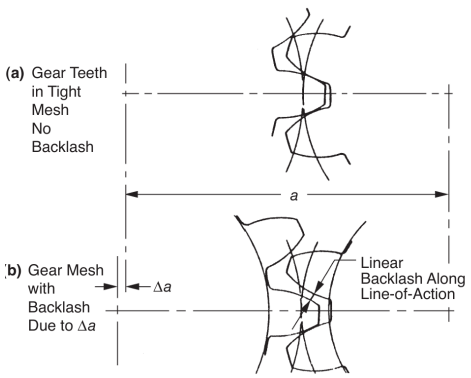

(a) Backlash Caused by Opening of Center Distance

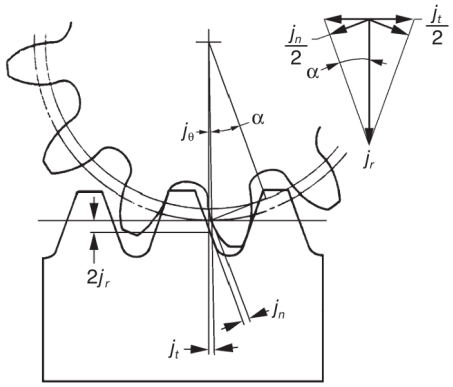

(b) Different definitions of backlash

Figure 2.6

It is possible to define different types of backlash, depending on the direction in which it is measured: circular backlash j_t, normal backlash j_n, center backlash j_r, and angular backlash j_θ (°). Their geometrical representation is shown in Figure 2.6b.
The geometrical correlation between the different types of backlash strongly depends on the type of gears employed. In this case, spur gears are used, and the corresponding relationships are presented below:

$$\begin{cases} j_n = j_t \cos\alpha & [\text{mm}] \\ j_r = \dfrac{j_t}{2\tan\alpha} & [\text{mm}] \\ j_\theta = \dfrac{j_t}{r} & [\text{rad}] \end{cases}$$

Where α is the gear pressure angle and r is the gear's pitch radius.
In order to define the relationship between the gear center distance and the angular backlash, it is first necessary to introduce one final definition of backlash: the linear backlash measured along the pitch circle j (see Figure 2.7 for a schematic representation).

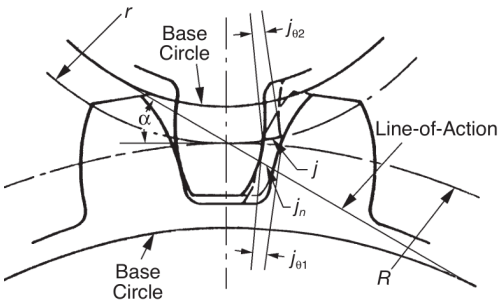

Figure 2.7: Geometrical Definition of Backlash

Geometrical considerations yield:

$$j = \frac{j_n}{\cos\alpha}$$

When the center distance is increased by an amount Δa, a backlash clearance develops between the mating teeth. The relationship between the center distance increase Δa and the normal backlash j_n (measured along the line of action) is given by:

$$\Delta j_n = 2\Delta a \sin\alpha$$

In the EMA test bench described in this section, the configuration is shown in Figure 2.8. The vertical distance $y_c = 68.06$ mm between the two mating gears is

known and fixed by design, while the horizontal distance x_c is adjusted through the micro-mover. The resulting distance between the gear centers can then be trivially determined from the Pythagorean theorem:

$$a = \sqrt{x_c^2 + y_c^2}$$

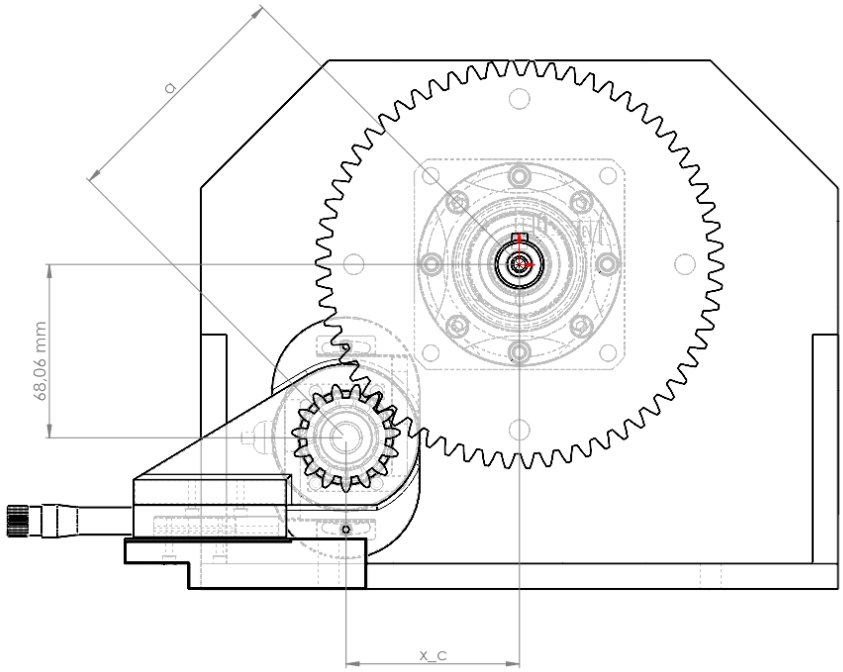

Figure 2.8: Backlash adjustment in EMA test bench

2.2 Braking Module

The braking module is designed for the experimental investigation of different friction conditions in the actuation system, with the aim of analyzing phenomena such as stick-slip, also in combination with backlash effects. Moreover, this module is generally capable of generating a variety of opposing load conditions. It can be broadly divided into two main parts: the braking shaft assembly and the chain-drive transmission.

2.2.1 Braking Shaft Assembly

The torque taken from the motor output shaft is transmitted to a parallel shaft via a sprocket–chain–sprocket system (described in section 2.2.2). On this shaft, the braking disc is mounted, representing the rotating component of the braking assembly. Adjacent to the braking disc, a metal plate is fixed to the brake shaft by means of two self-centering bearings. All static components of the braking assembly are mounted on this plate. In particular, a support manufactured using FDM is attached to the steel plate, carrying the brake micro-mover, the dedicated servo-actuator, and the brake caliper.
One important feature of this plate is that it is free to rotate within its plane and is connected to the bench via a plastic rod, which is linked to a load cell through a hinge. In this configuration, when the servo-actuator pushes the brake pad against the rotating disc—thus generating a braking moment—an equal and opposite moment is applied to the metal plate. As the plate rotates, it exerts a force on the load cell.
Knowing the geometrical dimensions involved, it is therefore possible to reconstruct the braking moment from the measurements provided by the load cell. The servo-actuator responsible for moving the brake pad against the disc generates the braking force. It was therefore necessary to adopt a servo-actuator capable of providing sufficient force while also responding promptly to variations in the required load. The actuator selected for this purpose is the SAVOX SC-0254MG, whose datasheet is presented in Table 2.7.

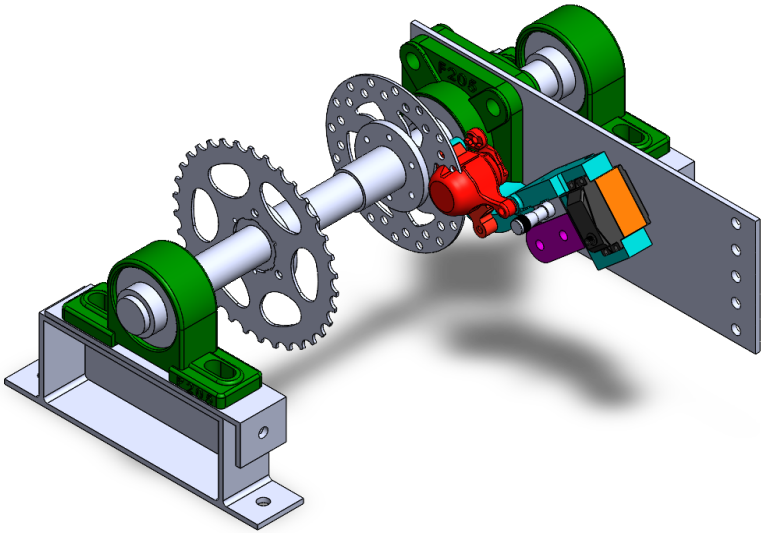

Figure 2.9: Braking Shaft Assembly

Speed 60°/Sec @ 4.8V	0.19
Speed 60°/Sec @ 6.0V	0.14
Torque (kg/cm) @ 4.8V	6.9
Torque (kg/cm) @ 6.0V	7.2
Rated Current (mA)	240
Blocking Current (mA)	1500
Weight (g)	49
Dimensions (mm)	W: 19.6; H: 39.4; D: 40.7

Table 2.7: SAVOX SC-0254MG datasheet

2.2.2 Chain drive transmission

In order to ensure the mechanical connection between the actuator module and the braking module, a chain-drive transmission is employed. This type of transmission provides low internal friction and represents a well-established system for installation and testing. Mounted on the output shaft of the electric motor, it adequately reproduces the dissipative effects typically present in an actuator gearbox. Furthermore, the characteristics of the two sprockets (summarized in Table 2.8) result in a transmission ratio of approximately 1.48, thereby generating

a higher torque on the braking shaft.

Driving gear	
Diameter	90 mm
Number of teeth	23
Driven gear	
Diameter	142 mm
Number of teeth	34

Table 2.8: Sprocket characteristics

Chapter 3

Simulink model description

Modeling and simulating physical systems offers the advantage of deepening the understanding of the underlying phenomena, while also enabling the testing of different physical conditions—including extreme cases—without risking damage to the experimental equipment. Moreover, as previously introduced, a sufficiently accurate model can greatly contribute to the analysis of potential failure modes in the real system and—if adequately fed with real input data and correctly validated—can also open promising prognostic perspectives.
The developed model aims to reproduce the standard operating conditions of the EMA test bench described in the previous chapter, while also incorporating the capability to simulate different fault scenarios within the system.

To reproduce the system dynamics over long time intervals while minimizing memory usage, a fixed-step explicit integration method was selected (ODE1—Euler's method). In order to adequately capture the reaction times typical of primary and secondary flight controls, and considering the system's characteristic time constants, an integration step of 1×10^{-6} s was adopted. As is common practice in this field, the time step was chosen to be one or two orders of magnitude smaller than the fastest characteristic time—in this case, the electrical dynamics.

At a macroscopic level, the model can be described by the following flow of information: the commanded position signal enters the Control Electronics Subsystem, where a control action is processed by means of a PID controller through the outer feedback loop, which includes the motor's position and speed. This control action takes the form of a reference current I_{ref}, which serves as the main input for the subsequent Inverter Model Subsystem. Here, together with the rotor angular position (obtained from the motor angular position via the resolver subsystem), three voltages—phases A, B, and C—are generated at each time step through Pulse Width Modulation (PWM), thereby correctly supplying the three phases of the

Electric Motor.
In the BLDC electromagnetic model, the currents in the three motor phases are computed using three star-configured RL Simscape branches, based on the applied phase voltages and the motor's angular state. From these currents, the total electromagnetic torque is calculated and transmitted to the motor–transmission dynamic model, where the mechanical dynamics are reproduced. This model outputs both the motor's angular state—fed back into the previously described control loops—and the actuator's angular position, obtained through the gearbox reduction ratio.

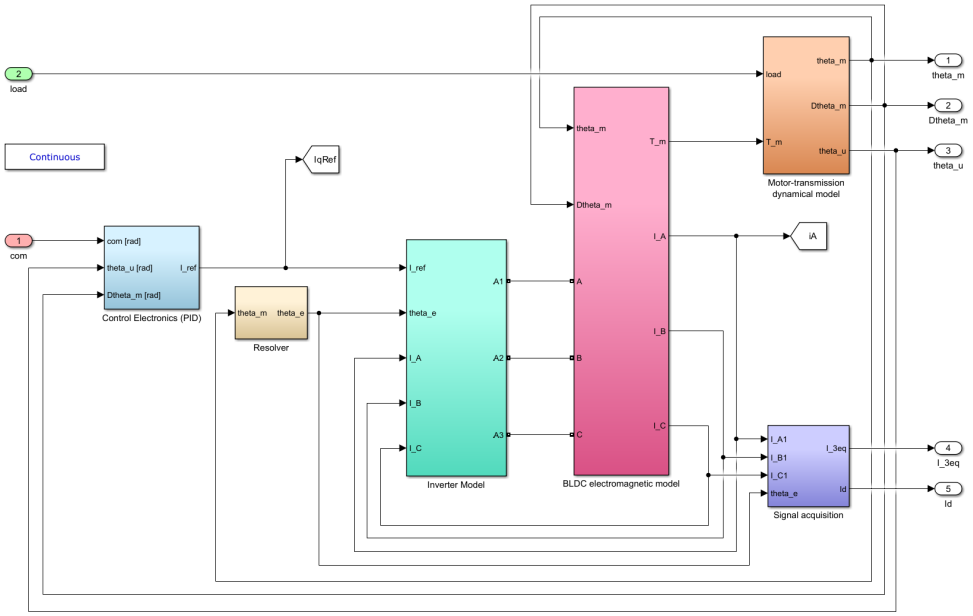

Figure 3.1: Model overview

3.1 Control Electronics

In this subsystem, a position error is first generated by subtracting the actual motor position from the commanded position. This error is then multiplied by a physical gain to obtain a reference speed, which is subsequently saturated. A speed error is computed by subtracting the actual motor speed from the saturated reference speed. The resulting speed error, together with the actual speed and the position error, is then fed into the PID controller.
The output of the PID controller defines the reference torque required from the motor. This torque is then divided by the motor's torque constant to obtain the reference current, which is subsequently saturated before being passed to the next subsystem.

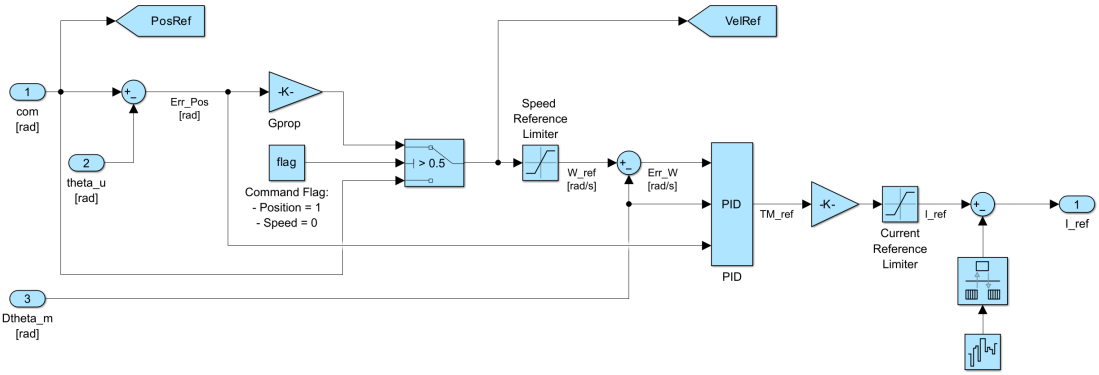

Figure 3.2: Control electronics subsystem

3.1.1 PID controller

The PID controller acts primarily on the position error, while the other two inputs are used to implement three different anti-windup strategies. While the proportional branch consists of a simple proportional gain, the derivative branch employs a derivative filter in its transfer function, as is common practice in this type of controller:

$$G_d(s) = \frac{T_d s}{\frac{T_d}{N} s + 1}$$

Finally, the integrative branch makes use of the continuous-time integrator provided in Simulink and, as previously reported, employs three different anti-windup strategies to prevent well-known control issues when dealing with saturation and hard stops.

- **Anti-windup 1**: the integrator branch is disabled when the motor speed remains zero for more than one integration step.
- **Anti-windup 2**: the integrator branch is disabled when the position error exceeds a predefined threshold.
- **Anti-windup 3**: the integrator gain is reduced proportionally to the difference between the saturated and unsaturated output signals.

It should be noted that, although a manual switch is included in the model—allowing the user to select either anti-windup method 1 or 2—the third method is always active, as it represents the most robust solution.

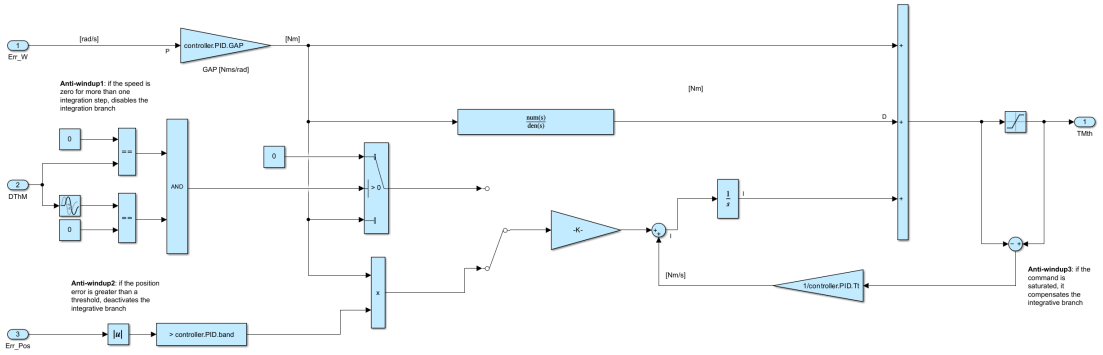

Figure 3.3: PID controller

3.2 Resolver model

The resolver subsystem consists of a single MATLAB Function block that computes the electrical angular position θ_e from the mechanical angular position of the motor shaft θ_m and the number of pole pairs p. The adopted formula is based on the simple relation

$$\overline{\theta}_e = \theta_m \cdot p$$

and subsequently applies the floor function to constrain the output within the range $[0, 2\pi)$:

$$\theta_e = 2\pi \left[\frac{\overline{\theta}_e}{2\pi} - \texttt{floor}\left(\frac{\overline{\theta}_e}{2\pi} \right) \right]$$

3.3 Inverter model

In the inverter subsystem, the reference current and the electrical angular position are first used to compute the three phase reference currents I_A, I_B, and I_C for the Electric Motor. This is achieved by applying the Inverse Clarke–Park transformations. For clarity, a more detailed explanation of the Clarke–Park transformations will be provided in Section 3.6, when the direct transform is introduced.
Once the three reference currents are computed, each is compared with the actual phase current of the corresponding phase, and the resulting current errors are sent to the Hysteresis PWM subsystem. In this subsystem, three Simulink Relay blocks are employed to convert the error signals into boolean outputs: a value of 1 is generated when the current error for a given phase reaches $+0.1\,\text{A}$, and 0 when it reaches $-0.1\,\text{A}$.

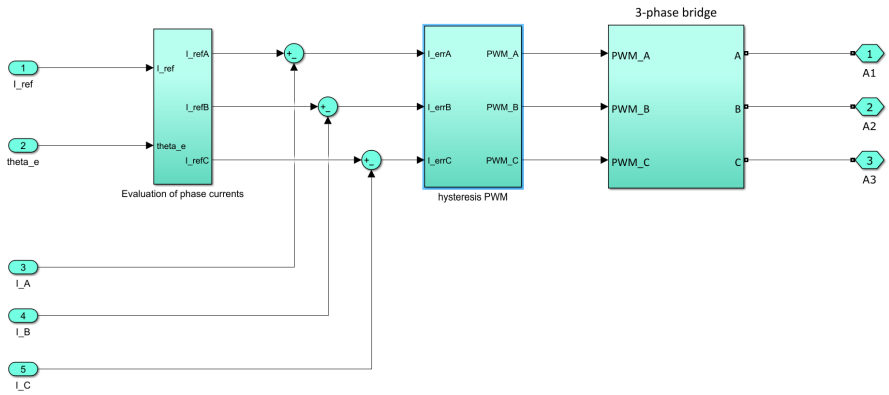

Figure 3.4: Inverter subsystem

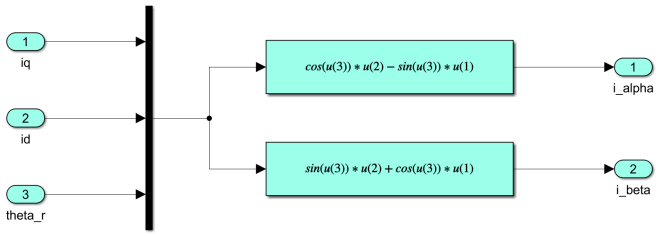

Figure 3.5: Inverse Park transform

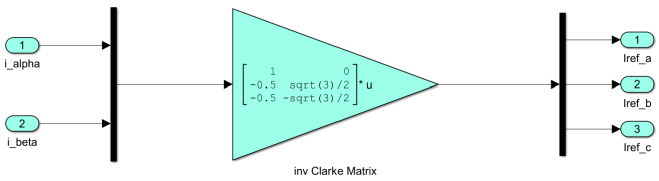

Figure 3.6: Inverse Clarke transform

Then, the three PWM signals—together with their inverse values—are sent to a Simscape MOSFET Universal Bridge block, which acts as a three-phase bridge controlling the electrical power that, in the real system, is supplied by the inverter module. This block outputs the three voltages, denoted as A, B, and C, which - in the physical system - are applied to the terminals of the motor phases.

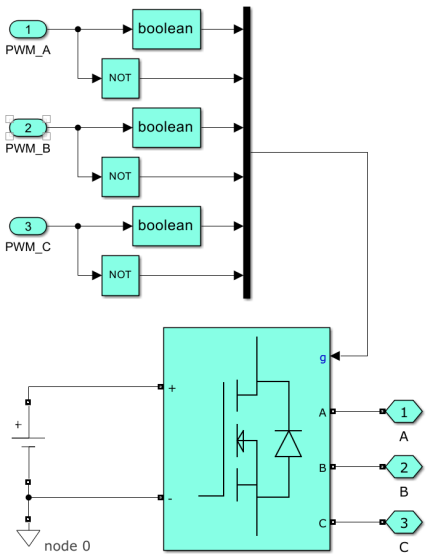

Figure 3.7: Three-phase bridge

3.4 BLDC Electromagnetic model

In the "BLDC Electromagnetic Model" subsystem, the first part of the model is dedicated to computing the back Electromotive Force (back-EMF) coefficients. These coefficients are used both for the calculation of the EMF itself and—since it can be demonstrated that they numerically coincide with the torque gain coefficients—for determining the torque contributions of each phase based on the three phase currents.
The model also implements three blocks named "Effect of Static Eccentricity," which account for possible phenomena such as partial stator coil short circuits or the influence of rotor static eccentricity. These corrections are applied to the nominal back-EMF coefficients, which are instead derived from the rotor's electrical angle through the "Effect of Rotor PM Field Density" blocks.
The back-EMF coefficients are then multiplied by the motor speed, yielding the three back-EMF voltages to be applied to each phase. In the "Three Phase RL Model" subsystem, three star-connected RL branches are implemented using Simscape blocks, all sharing a common negative pole and subjected to their corresponding supply voltage and back-EMF. In this way, the actual currents circulating in each phase can be determined. These currents are fed back to the Inverter Model, as previously described, and subsequently used in the "Computation of motor torque" subsystem to calculate the torque contributions of each phase by multiplying each current by its corresponding back-EMF coefficient. These contributions are then summed and multiplied by a factor of $\sqrt{2}$ in order to convert the torque obtained

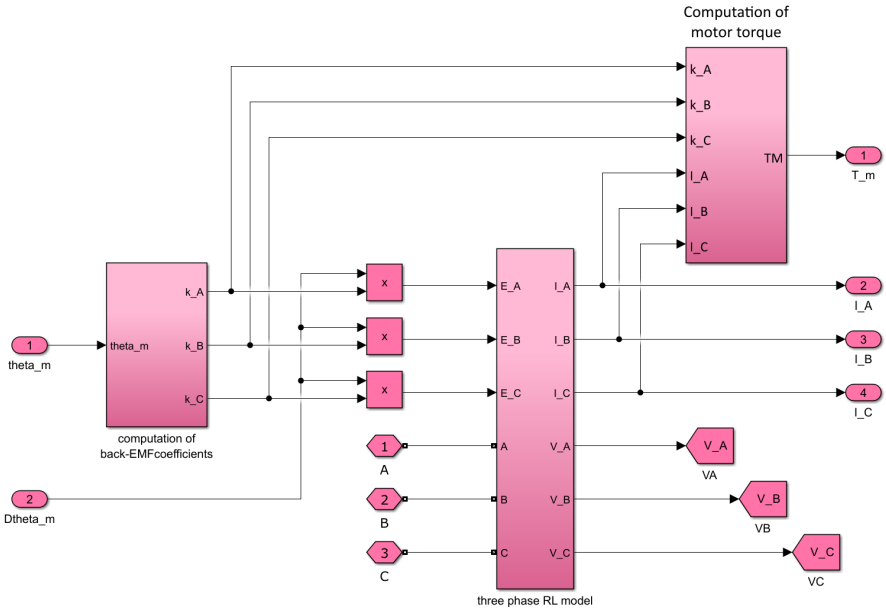

Figure 3.8: BLDC Electromagnetic model

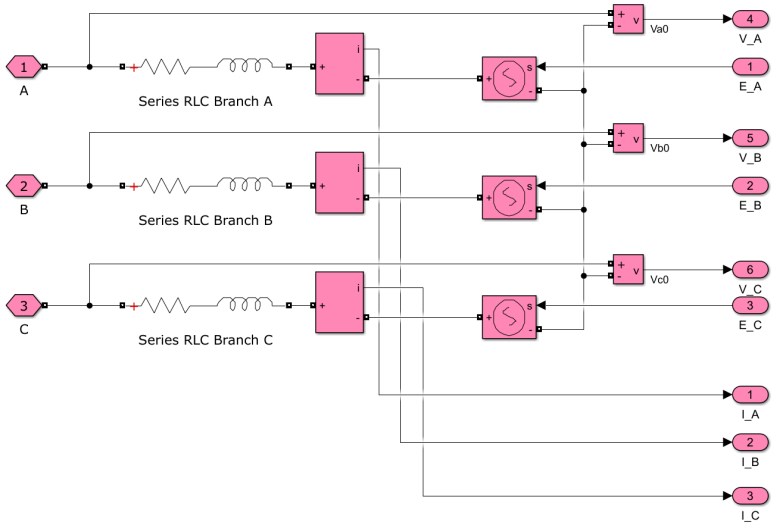

Figure 3.9: Three-phase RL model

from Root Mean Square (RMS) form to the peak value form.

3.5 Motor-transmission dynamical model

The "Motor–Transmission Dynamical Model" subsystem represents the core of the system's mechanical dynamics. Receiving the actual motor torque as input, it simulates the behavior of the motor–transmission assembly. The net torque is first calculated by subtracting from the torque generated by the electric motor the opposing viscous torques of both the motor and the load, as well as the friction torque derived from the Borello Friction Model. From an overall perspective, this net torque is divided by the moments of inertia of both the motor and the load (appropriately converted to their fast-shaft values) and then integrated twice to obtain the motor's angular position. This value is subsequently multiplied by the reduction ratio to yield the angular position at the output shaft of the gearbox.
In practice, this subsystem implements several non-linear modeling techniques, including saturation ports, state ports, event-based logical conditions, and—most importantly—the Borello Friction Model itself, which will be described in detail in the following pages.

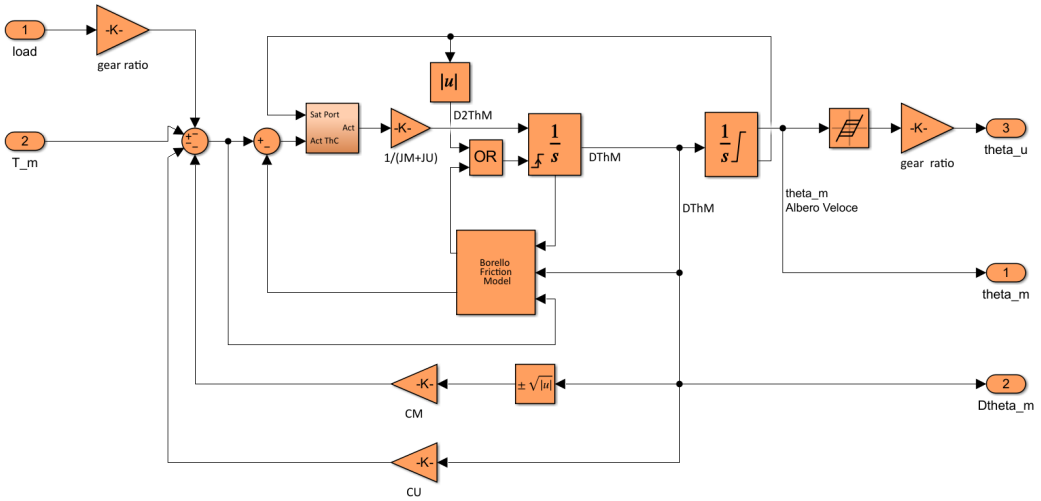

Figure 3.10: Motor-transmission dynamical model

3.5.1 Borello Friction Model

The three inputs of the Borello Friction Model (BFM) are: the net torque (excluding friction), the motor shaft angular speed, and the output of the first integrator's state port. It should be noted that, under normal (non-reset) conditions, the state port provides the regular output of the integrator. In the event of an external reset, however, it outputs the non-reset value at the current time step. This feature is particularly useful for avoiding algebraic loops when the integrator output is

employed as part of an external reset condition for the same integrator.
The BFM is an event-based algorithm that exploits the zero-crossing of the velocity to discriminate between static and dynamic friction conditions. Static friction is modeled according to Coulomb's friction law, i.e., by computing a torque opposing the applied torque, with a magnitude equal to the minimum between the static friction threshold and the applied torque itself.
Dynamic friction, on the other hand, is modeled as a torque opposing the shaft speed, with a magnitude equal to the dynamic friction derived from the dynamic friction coefficient.

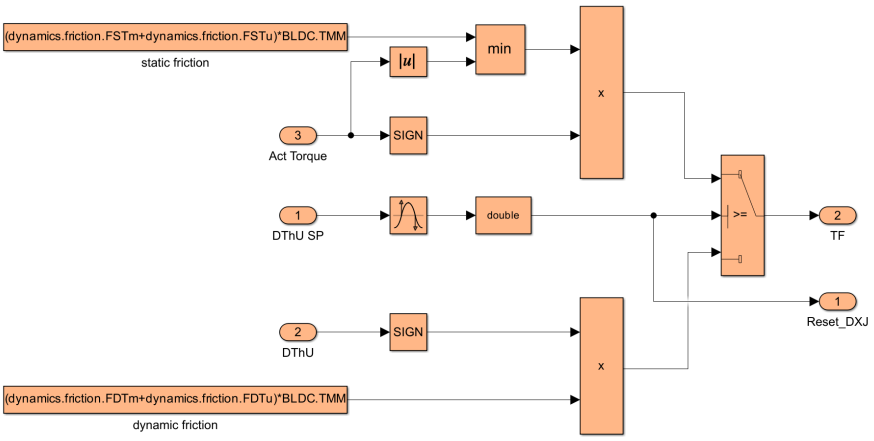

Figure 3.11: Borello Friction Model

If, for example, the shaft is in motion and a zero-crossing in velocity occurs, the BFM evaluates the static condition. The system dynamics then determine whether the shaft has come to rest or is simply reversing its direction. This evaluation is performed by the central branch of the model through a Simulink logical switch.
At the same time as the zero-crossing, a reset signal is generated to reset the integrator that computes the velocity. As will be explained in greater detail later in this chapter, this is not the only reset condition implemented for handling stop conditions.

3.5.2 Velocity Integrator Reset Conditions

In order to correctly explain the reset conditions of the integrator responsible for calculating the motor shaft velocity, it is necessary to distinguish between the two types of stops implemented, since both must trigger a reset of the velocity integrator, albeit for different reasons.
A dynamical stop occurs when the shaft comes to rest due, for example, to friction

forces. A hard stop, on the other hand, takes place when the system reaches its positive (or negative) end stop and, at the same time, a torque continues to act in the direction of that limit.
The former is handled by the reset signal generated as one of the outputs of the BFM subsystem (as described in Section 3.5.1). The latter, instead, is managed as follows: when the position integrator becomes saturated, the signal from its saturation port switches from a boolean 0 to 1 if the upper saturation limit is reached, or to -1 if the lower saturation limit is reached. This signal is then used in two ways. First, its absolute value (to account for both saturation conditions) enters an OR logical condition together with the reset signal from the BFM, ensuring that the velocity integrator is correctly reset. Second, it is fed into a logical block that evaluates whether the net torque is pushing the shaft against the end stop. This is done by comparing the signs of the saturation signal and the net torque: if they match, the net torque is set to zero until one of the two signs changes.
In this way, not only is the velocity integrator reset to zero, but it also maintains this zero value, since it continues integrating a net torque equal to zero.

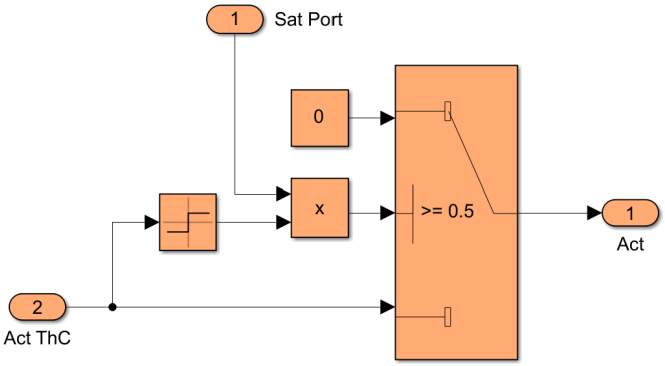

Figure 3.12: Hard stop logic block

3.6 Signal acquisition

The signal acquisition subsystem is responsible for converting the three phase currents I_A, I_B, and I_C into the direct and quadrature currents I_d and I_q through two subsequent transformations, known as the Clarke–Park transformations, as well as for performing a final filtering stage required to remove the noise generated within the Electromagnetic Model during the simulation.

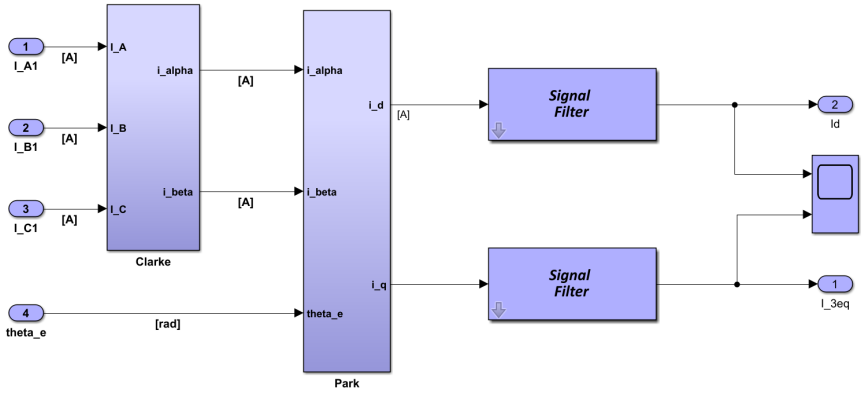

Figure 3.13: Signal Acquisition Subsystem

The Clarke transformation is essentially a geometrical relation that, leveraging the symmetry of the stator model (in this case, three evenly spaced star-connected RL branches), converts the three phase currents into two currents, I_α and I_β, on a fixed reference frame at each time step.
This is achieved by decomposing the three phase currents, considering that the branches are spaced by $\frac{2}{3}\pi$ radians.

$$\begin{Bmatrix} I_\alpha \\ I_\beta \end{Bmatrix} = \frac{2}{3} \begin{bmatrix} 1 & -\frac{1}{2} & -\frac{1}{2} \\ 0 & \frac{\sqrt{3}}{2} & -\frac{\sqrt{3}}{2} \end{bmatrix} \begin{Bmatrix} I_A \\ I_B \\ I_C \end{Bmatrix}$$

The Park transformation, in turn, converts the two fixed-frame currents I_α and I_β into the direct and quadrature currents, I_d and I_q, defined on a rotating reference frame locked to the rotor. This is achieved through a simple rotation matrix around the rotor shaft of an angle equal to the electrical angular position θ_e. The direct current generates a component of the rotating magnetic field that is always aligned with the one produced by the rotor's permanent magnets. The quadrature current, on the other hand, generates a component of the magnetic field that—as the name suggests—is always in quadrature with respect to the rotor's magnetic field. The quadrature component is thus oriented in the direction that maximizes the motor

torque. This explains why, when the inverse Park transformation is applied in this model, the direct reference current is ideally set to zero.

$$\begin{bmatrix} I_d \\ I_q \end{bmatrix} = \begin{bmatrix} \cos\theta_e & \sin\theta_e \\ -\sin\theta_e & \cos\theta_e \end{bmatrix} \begin{bmatrix} I_\alpha \\ I_\beta \end{bmatrix}$$

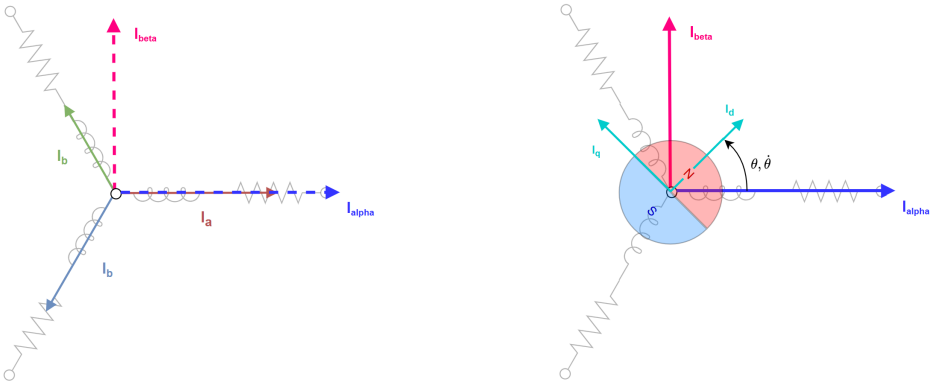

(a) Clarke transformation **(b)** Park transformation

Figure 3.14

Chapter 4

Activity description

The experimental activity on the EMA test bench described in this work was primarily aimed at implementing a set of hardware modifications, enabling its operation under the new configuration, and setting up a test campaign for model validation.

4.1 Main hardware modifications

The test bench described in the previous section represents the current state of the system. This section presents the main improvements introduced with respect to the original configuration.

4.1.1 Gearbox Assembly

As previously discussed, due to several limitations—such as the low torsional stiffness that required a high-fidelity model, and the difficulty of accurately analyzing backlash due to internal clearances in the legacy planetary gearbox—the original FDM-manufactured unit was replaced with a Tramec commercial gearbox, presented in section 2.1.5.

The new gearbox is mounted on a dedicated steel support and connected to the motor via a shaft–jaw coupling system. In particular, both the shaft and the inner coupling element were 3D-printed via FDM. This design choice introduces new research opportunities, as adjusting printing parameters such as infill density, internal geometry, and filament material allows one to tune key physical properties of the transmission, namely the torsional stiffness k (via the shaft), damping coefficient c (via the coupling), and transmission inertia.
To mitigate the risk of delamination or detachment during operation, a custom-designed shaft guard was developed and installed.

On the gearbox support, a custom mount for the encoder gear was also designed. As previously described, this enables backlash adjustment through a dedicated micromover. The selection of the gearbox and the meshing between its output gear and the encoder gear was made to preserve the overall reduction ratio between the motor output and the encoder, thus avoiding the need to re-validate the control algorithms implemented in the PLC and their integration with the simulation model.

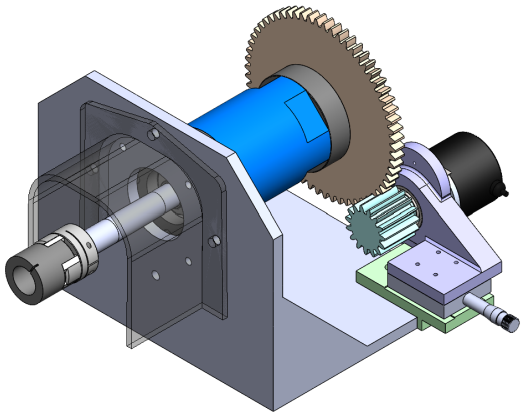

Figure 4.1: Gearbox-shaft-coupling assembly

4.1.2 Braking Assembly

The main modification to the braking assembly lies in the replacement of its support structure, which now also hosts a micromover (figure 2.9). This updated design extends the experimental capabilities of the braking group, enabling the application of braking via friction, not only through the servomotor but also via imposed axial displacement.

Additionally, the previous closed-loop control strategy (which regulated the braking torque based on data from the load cell) has been temporarily removed during this study, as it was difficult to implement and more suitable for simulating an opposing load than for replicating friction on the actuation line.

The friction torque is still reconstructed from the load cell readings downstream of the rotating plate structure described in section 2.2.1, acquired through an Arduino UNO connected to a dedicated interface device.

4.2 Test rationale and methodology

4.2.1 Test rationale

The rationale behind the test campaign lies in the characterization of the behavior of the EMA test bench and the validation of its Simulink model under various experimental conditions. These conditions are primarily determined by the linear displacement of the two micromovers previously described, and are designed to experimentally investigate two nonlinear phenomena that are typical of these actuation systems and have been discussed earlier in this work: friction/stick-slip effects and gear backlash.
These phenomena, which can occur simultaneously during real operation, are first studied independently in order to isolate their individual contributions, and subsequently analyzed in combination to observe their coupled effects on system dynamics

The brake micromover allows for the modification of the normal force between one of the brake pads and the braking disc. By adjusting this force through controlled linear displacement, the resulting friction torque applied to the transmission is varied.
Conversely, the encoder support micromover is used to vary the center distance between the gearbox's output gear and the encoder gear, as detailed in section 2.1.6. It is important to note that the encoder's measurements — affected by the resulting backlash—are part of the closed-loop position control performed on the motor by the virtualized PLC.

More broadly, the overall objective of the test campaign is to investigate the behavior of an all-electric actuation system, assess its reproducibility under controlled laboratory conditions, and explore its nominal performance across different transmission scenarios. Additionally, the campaign aims to validate the simulation model, laying the groundwork for future model-based prognostic capabilities.

4.2.2 General architecture and methodology

In this section, a more in-depth description of the test bench architecture (schematically illustrated in Figure 4.2) is provided, followed by an explanation of the methodology adopted for the test campaign.

Power to the bench is supplied by two separate AC sources. The 380V three-phase outlet—safely routed through an emergency stop button—feeds the inverter, which in turn supplies the motor phases. The 220V outlet is converted to 24V DC by an AC/DC converter; this voltage is used to power the Microbox PC (via the Control Unit), which runs the virtualized PLC. From the same 24V line, additional DC/DC

converters provide power to the brake servomotor (via the Arduino Interface Board) and to the encoder.

The virtualized PLC is launched on the Microbox PC, which is connected to the Control Unit via Ethernet. The same Ethernet network also connects a second PC, which plays a dual role:

- It runs SIEMENS SIMATIC STARTER to monitor and log system variables such as motor and encoder positions, phase currents, and other relevant signals.
- It executes a custom MATLAB acquisition script to collect data from the load cell. The load cell is connected to the Arduino Interface Board, which transmits the data to MATLAB via the PC's internal serial communication port.

Additionally, this second PC is used to send the commanded position to the Control Unit wirelessly through a local server.

Once the setup is complete and the command is properly issued, the actuator begins to follow the commanded position, as controlled by the PLC. At the end of the operation, the STARTER software allows the user to export the recorded system variables to a `.csv` file. Simultaneously, the output from the MATLAB acquisition script—containing the readings from the load cell—is made available.

These two files serve as input for the Data Handling MATLAB Script, which performs the following tasks:

- Imports and organizes data from both the `.csv` and `.mat` files into a structure object.
- Corrects motor and external encoder signals to compensate for multi-turn errors,
- Synchronizes motor and load cell data using the trigger signal sent from the Arduino board to the Control Unit and logged on the `.csv` file
- Converts raw data into consistent units, trims the time window to isolate the test interval, and computes both the command frequency and phase
- Computes the friction torque by processing the force data acquired from the load cell

The data flow described above is schematically illustrated in Figure 4.3, which also includes a representation of the output structure containing all the test data.

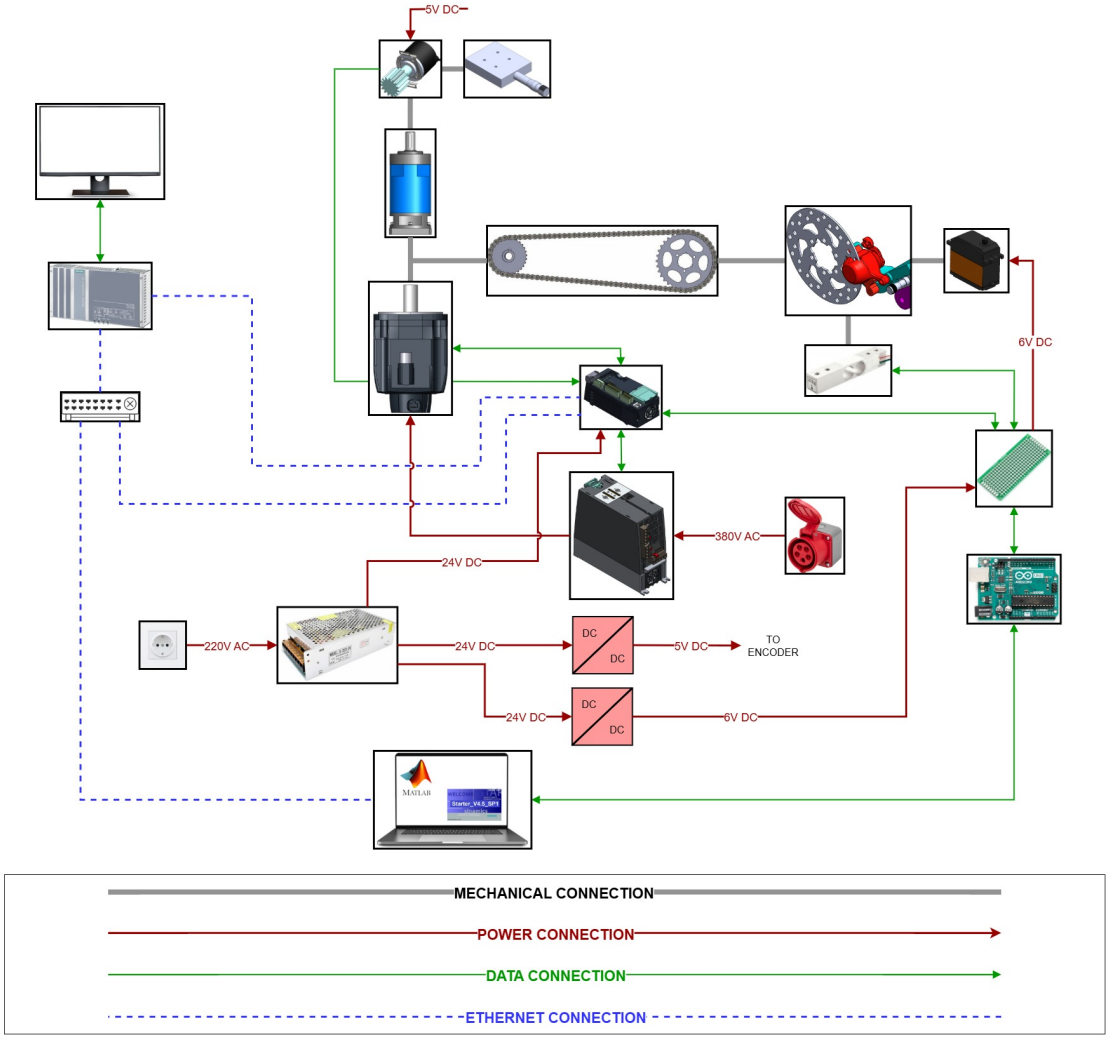

Figure 4.2: Test bench architecture diagram

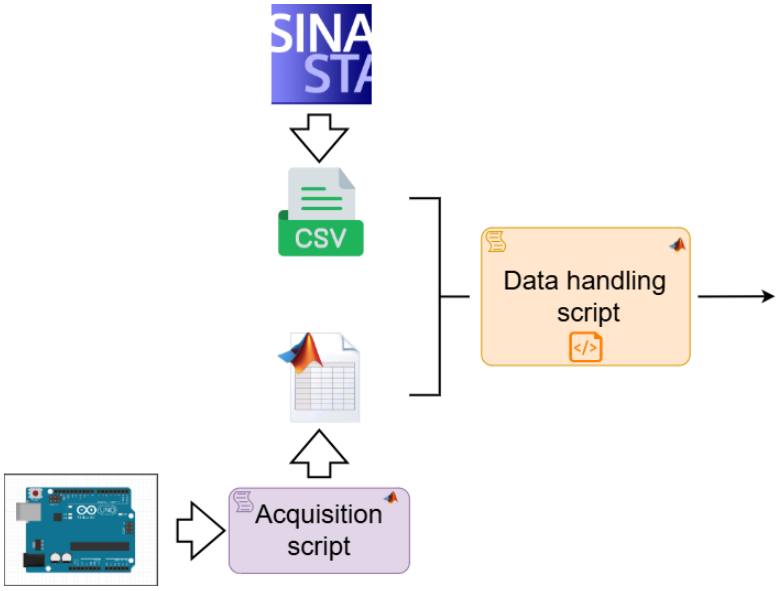

OUTPUT DATA	
Variable	Description
time	Time
posEncoder	Encoder position
posMotor	Motor position
velCom	Commanded velocity
velRead	Measured velocity
IU	Phase u current
IV	Phase v current
IW	Phase w current
friction	Friction torque
amplCom	Amplitude of command
freqCom	Frequency of command
com	Command value

Figure 4.3: Test bench data flow diagram

Chapter 5

Experimental work

In this chapter, the experimental methodology adopted during the test campaign will be illustrated. As previously discussed, the primary method employed to vary the system configuration during the experimental phase involves two independent linear displacements, implemented via separate micro-movers. Therefore, it is essential to properly zero and calibrate each device to ensure that—once a reference position has been established—the relationship between displacement and the corresponding operating variable (i.e., friction force measured by the load cell, and angular backlash at encoder gearing, respectively) is well-defined and accurately quantified.
To this end, two mapping procedures—one for each micro-mover—were conducted and are described below, along with the results obtained.

5.1 Load Cell Mapping and Calibration

In order to identify the zero position of the brake micromover—defined as the position of non-contact from which any further linear displacement would generate adhesion between the brake pad and the disc—a simple yet effective ink-based method was employed. Specifically, a section of the disc was marked with a thin layer of ink, and a low-slope ramp position command was issued to the actuator. In this way, the linear displacement corresponding to the first contact between the pad and the disc could be detected by observing the removal of ink. Once identified, this position was referenced to a displacement of 2 mm on the micromover, thereby enabling a controlled 2 mm operating range. In this configuration, a 2 mm displacement on the micro-mover corresponds to the non-contact condition, while 0 mm represents the maximum admissible contact between pad and disc.
Once the preliminary setup was completed, the mapping phase for the load cell began. A reference angular velocity of 0.085°/s on the gearbox output shaft was

selected for the characterization tests, as it was deemed sufficiently representative of the operating speeds employed in the experimental activities object of this study. It is important to note that, in this phase, only dynamic dry friction is assumed to be present. Therefore, the choice of the reference velocity can be considered arbitrary, as this phenomenon is generally independent of speed.

The selected displacement range was subsequently divided into 0.1 mm increments, and a 120-second test was performed for each position. The data acquired from the Arduino script were stored and subsequently processed using a dedicated data-handling routine. Figure 5.1 illustrates the measured force under three significant conditions: zero dry friction (corresponding to a 2 mm displacement of the micro-mover), intermediate friction (1 mm displacement), and maximum friction (0 mm displacement). A small measurement bias was corrected, mainly attributed to residual viscous friction and sensor offset. Consequently, only dry friction was considered in the analysis.

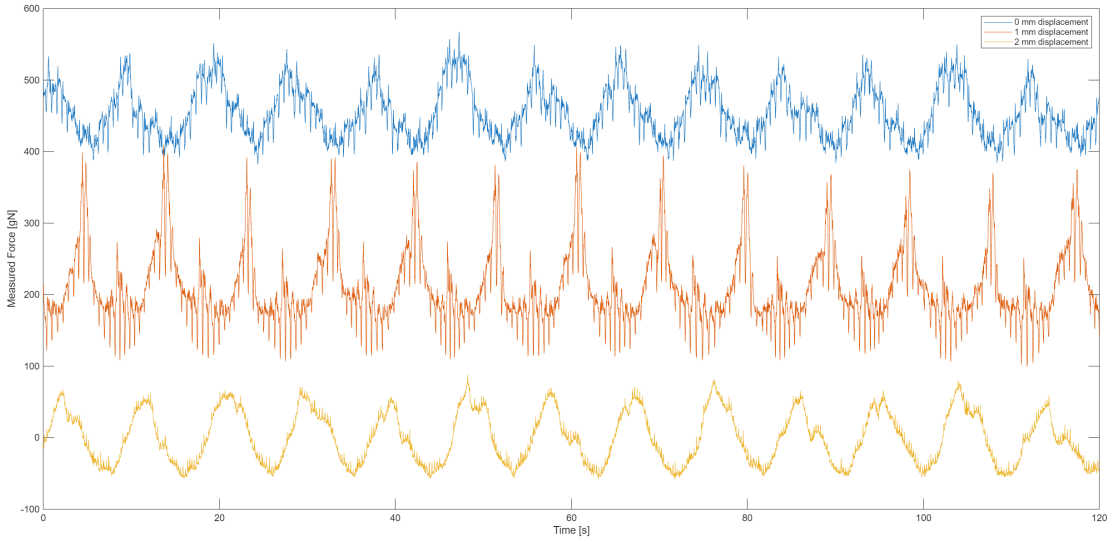

Figure 5.1: Measured load trends under three friction conditions

According to the system's rotational dynamics, the force measured by the load cell exhibits a periodic behavior around a mean value. This representative mean value is used to extrapolate the mapped trends discussed in Chapter 6, and is reported in Table 5.1, together with the corresponding friction torque.
The reconstruction of the friction torque T_f from the load cell measurements is straightforward and can be performed by balancing the total torque acting on the rotating plate. The lever arm x_{lc} measured from the center of rotation to the load cell, is equal to 0.233 m, while the force F_{lc} measured by the load cell

in gN is converted to Newtons by multiplying by a factor of $g/1000$. Finally, to express the torque at the motor output shaft, the obtained torque is divided by the chain–sprocket transmission ratio $\tau_s = \frac{34}{23}$.

$$T_f = \frac{F_{lc}\ x_{lc}\ g}{1000 \cdot \tau_s}$$

Displacement [mm]	**Force [gN]**	**Torque [Nm]**
2.0	0	0
1.9	3.0577	0.0047279
1.8	8.3614	0.012929
1.7	23.315	0.03605
1.6	43.6995	0.067569
1.5	60.3011	0.093239
1.4	79.5809	0.12305
1.3	106.7966	0.16513
1.2	132.3573	0.20465
1.1	185.6327	0.28703
1.0	209.0598	0.32325
0.9	230.1396	0.35585
0.8	249.9375	0.38646
0.7	272.5833	0.42148
0.6	295.2194	0.45648
0.5	338.5649	0.5235
0.4	358.7146	0.55465
0.3	387.2421	0.59877
0.2	410.688	0.63502
0.1	438.3714	0.67782
0.0	453.3086	0.70092

Table 5.1: Load cell mapping - average force and torque values

Given the rich frequency content of the load-cell measurements, the variability in their waveform shapes, and the interest in investigating the harmonic behavior of the phenomenon, a spectral analysis was performed using Welch's method to estimate the Power Spectral Density [12].
Once the 0 Hz component—representing the periodic behavior around the mean value—was filtered out, it was observed that, for every test, the first three low-frequency peaks occurred at approximately the same frequencies. These peaks, which are integer multiples of each other, clearly correspond to different harmonics of the load-cell signal with respect to the excitation, i.e., the angular frequency of the motor, properly reported to the braking shaft through the chain-sprocket transmission ratio τ_s.

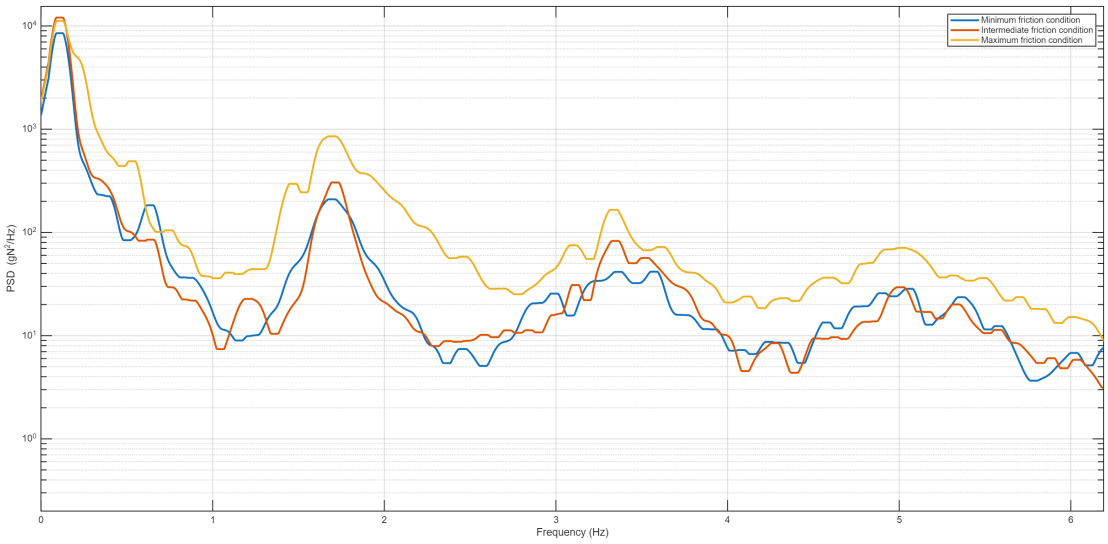

Figure 5.2: Spectral analysis of the measured loads - three limit friction conditions

5.2 Gear Backlash Mapping and Calibration

Analogously to the procedure adopted for the calibration of the load cell, a zero position for the backlash-regulating micro-mover was first established. This was accomplished by manually rotating the reducer output gear while adjusting the linear displacement of the encoder gear, bringing the two gears progressively closer. At the same time, the real-time trends were monitored using Siemens STARTER software, in order to identify the first micro-mover position that exhibited the minimum play between the two gears.
The selected zero-backlash position corresponded to a 13 mm reading on the micro-mover. Subsequently, a maximum-backlash position was identified by increasing the center distance between the meshing gears, without exceeding a limit at which tooth skipping could occur. This condition is particularly critical, since the position feedback loop relies on the external encoder output; a tooth-slip event could cause the electric motor to overcompensate for the sudden increase in position error, resulting in dangerously high currents and accelerations. The maximum-backlash condition was therefore set at a micro-mover displacement of 6 mm.
The selected position range was then subdivided into 0.5 mm steps, and the test command was established. Since gear backlash is primarily observed when the driving gear reverses its direction of motion, a sinusoidal input with an amplitude of 10 deg (referred to the slow shaft) and a frequency of 0.1 Hz was selected.
Using the selected command, a test was performed for each micro-mover position. Following the data flow described in the previous chapter, the data exported from Siemens STARTER were post-processed and synchronized through the dedicated data-handling script.

Backlash was analyzed by comparing the position readings from the two encoders in the system. The so-called motor position refers to the angular position measured by the encoder embedded in the electric motor on the fast shaft; for convenience, this value is scaled to the slow shaft by applying the TRAMEC gearbox reduction ratio (120), so that it can be compared with the encoder position, i.e. the position measured by the external encoder closing the feedback loop. This latter measurement is similarly referred to the reducer output shaft by applying the reduction ratio of the corresponding gear pair (62/15).

Figures 5.3, 5.4, and 5.5 show three representative results from the tests: the zero-backlash condition (corresponding to a 13 mm micro-mover displacement), an intermediate-backlash condition (9 mm), and the maximum-backlash condition (6 mm).

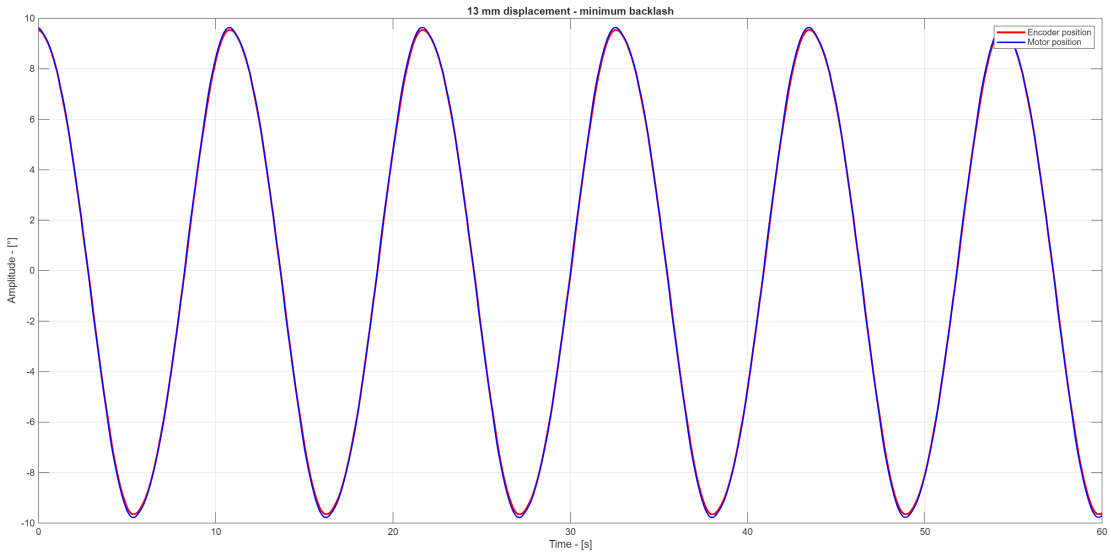

Figure 5.3: Motor and Encoder angular position - minimum backlash condition

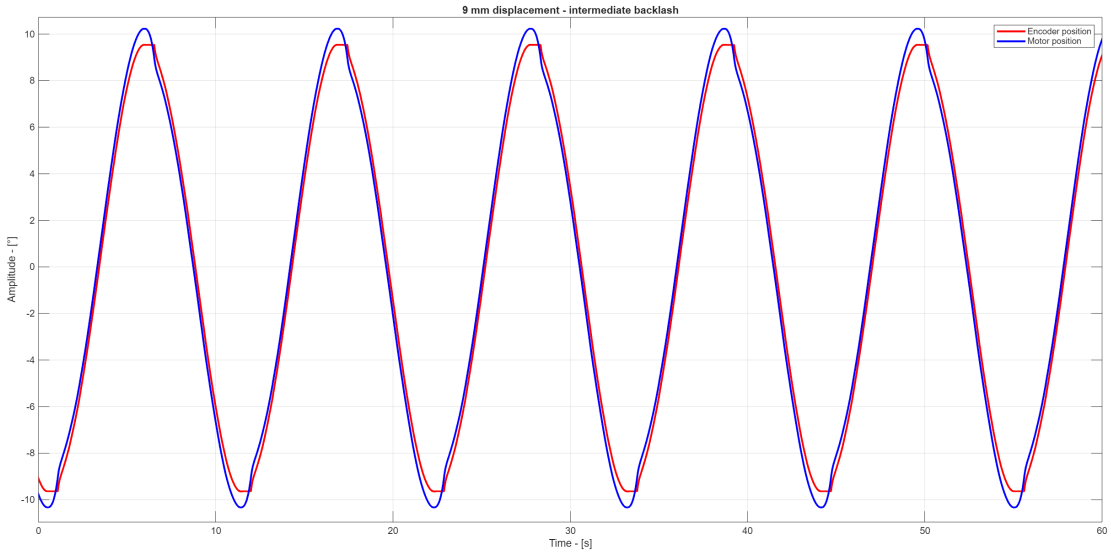

Figure 5.4: Motor and Encoder angular position - intermediate backlash condition

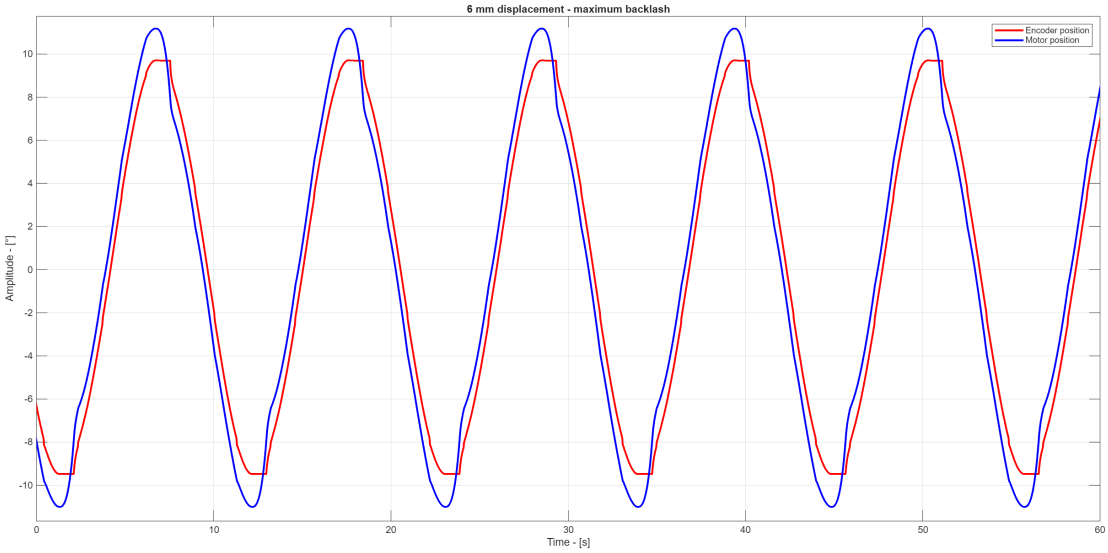

Figure 5.5: Motor and Encoder angular position - maximum backlash condition

It is worth highlighting some characteristic behaviors of backlash-affected systems that can be observed in the trends reported in this section. The first aspect to note is how the play in the position feedback loop influences the amplitude of the command executed by the electric motor. To compensate for the dead band, the control logic produces a sinusoidal motion of greater amplitude, as can be seen when comparing the zero-backlash and maximum-backlash conditions. Furthermore, this dead-band compensation is evident in the shape of the motor position, which exhibits a steeper descent near the instants at which the encoder gear comes to rest.

The backlash calculation for each test followed a straightforward approach based on the residual between the motor-encoder and external-encoder positions. To estimate the average backlash value associated with both the positive-to-negative and negative-to-positive motion reversals, the following procedure was adopted:

Algorithm 1 Backlash computation

1: **for** each test i **do**
2: compute residual $res(i)$
3: $backlash(i) \leftarrow \text{mean}\Big(|\max(res(i))|,\ |\min(res(i))| \Big)$
4: **end for**

Displacement [mm]	**Backlash [deg]**
13.0	0.16575
12.5	0.16608
12.0	0.16905
11.5	0.19871
11.0	0.22836
10.5	0.34330
10.0	0.46382
9.5	0.58029
9.0	0.70121
8.5	0.84340
8.0	0.98959
7.5	1.13980
7.0	1.30630
6.5	1.50050
6.0	1.78750

Table 5.2: Gear Backlash Mapping - angular backlash values

The backlash calculated for each displacement was then fitted with a trend, which is presented in detail in Chapter 6. Here, in Table 5.2, only the values corresponding to integer displacement positions are reported for clarity.

5.3 Comparison with the model results

In this section, the experimental procedure used to generate a restricted validation dataset, along with its subsequent comparison with the results of the mathematical model—described in detail in Chapter 3—are presented. Fifteen sampling points were selected with the aim of obtaining different combinations of gear backlash and resistive torque, in accordance with the characterization presented in this chapter.

Three levels of friction were selected: And five levels of backlash:

Friction level	**Friction torque [N · m]**	**Micro-mover 1 position [mm]**
Low	0	2
Medium	0.32325	1
High	0.70092	0

Table 5.3: Friction levels and corresponding conditions

Backlash level	**Backlash [deg]**	**Micro-mover 2 position [mm]**
Low	0.16575	13
Medium Low	0.16905	12
Medium	0.46382	10
Medium High	0.70121	9
High	0.98959	8

Table 5.4: Backlash levels and corresponding conditions

The sampling points obtained from the combination of these physical conditions were then indexed and are presented in Table:
The selected tests were then performed according to the experimental and data-handling procedure described in Section 4.2.2. Regarding the model simulations, the procedure was the following: In the test-bench data-handling script, the sinusoidal command is first reconstructed by means of an Fast Fourier Transform, which is used to determine its frequency and phase, while the amplitude is taken from the external encoder position signal. This reconstructed command, together with the experimentally measured backlash and load-cell force, is then used as input for the simulation. In the main simulation script, the remaining parameters—such as mechanical, electrical, and control-related quantities—are defined accordingly.

Next in this section, the comparison between the experimental and simulated results is presented, focusing on the variables of interest: encoder position, velocity, and quadrature (torque-generating) current.

Sample	**Friction level**	**Backlash level**
1	Low	Low
2	Low	Medium Low
3	Low	Medium
4	Low	Medium High
5	Low	High
6	Medium	Low
7	Medium	Medium Low
8	Medium	Medium
9	Medium	Medium High
10	Medium	High
11	High	Low
12	High	Medium Low
13	High	Medium
14	High	Medium High
15	High	High

Table 5.5: Enumeration of the 15 sampling points

For conciseness, only 9 out of the 15 sampling points—those considered most representative—are reported.

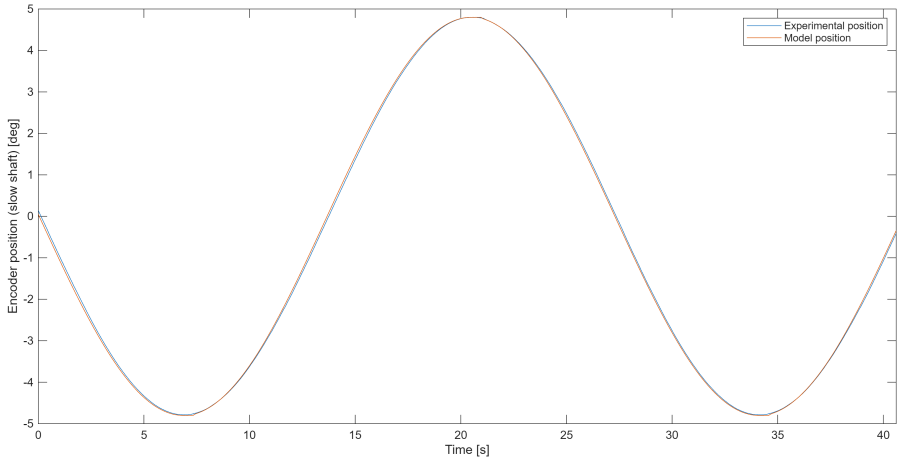

(a) Position

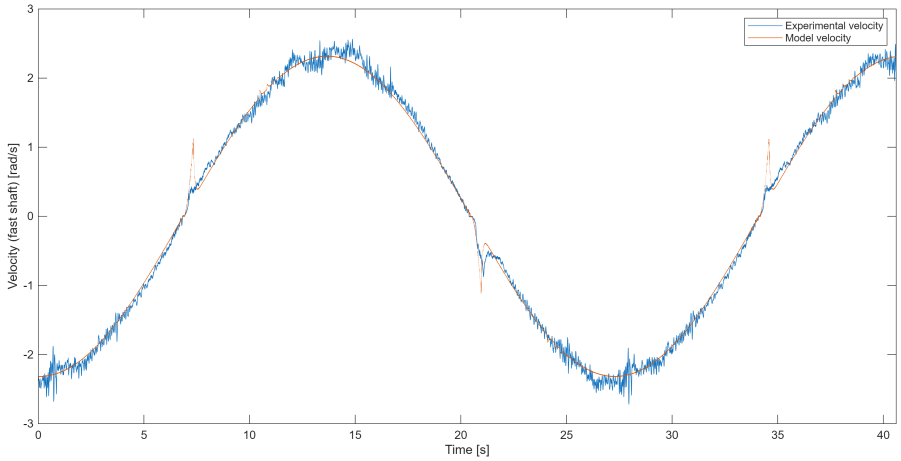

(b) Velocity

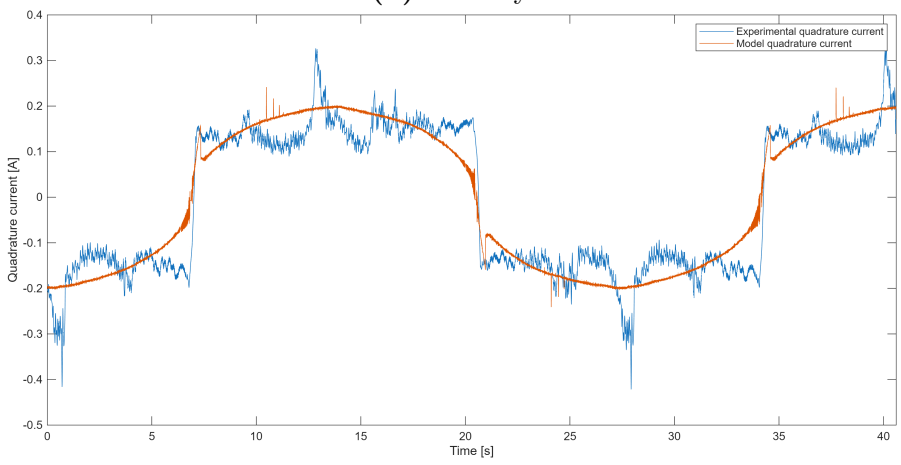

(c) Quadrature current

Figure 5.6: Experimental and simulated responses for Sample 1.

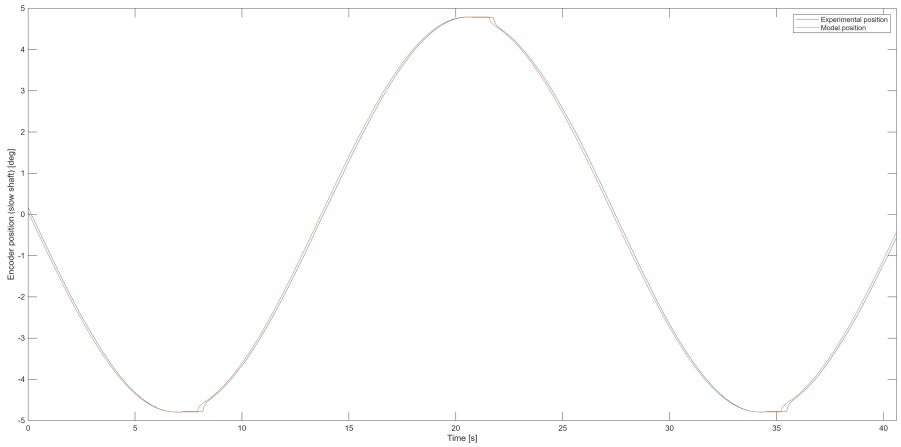

(a) Position

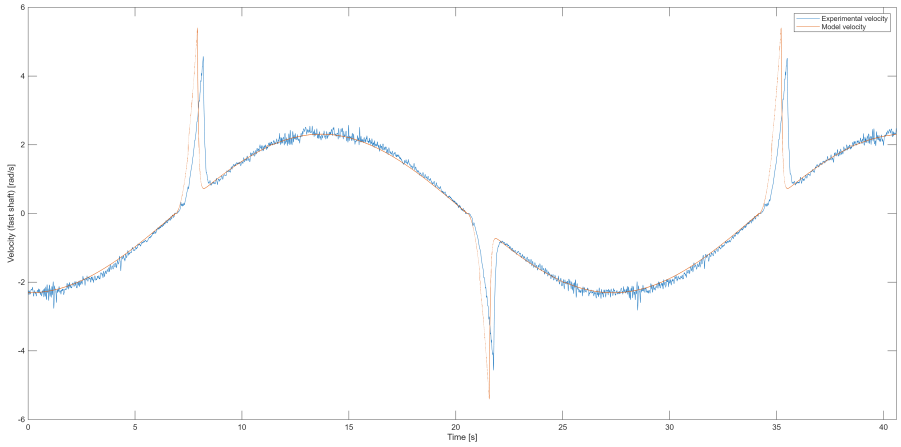

(b) Velocity

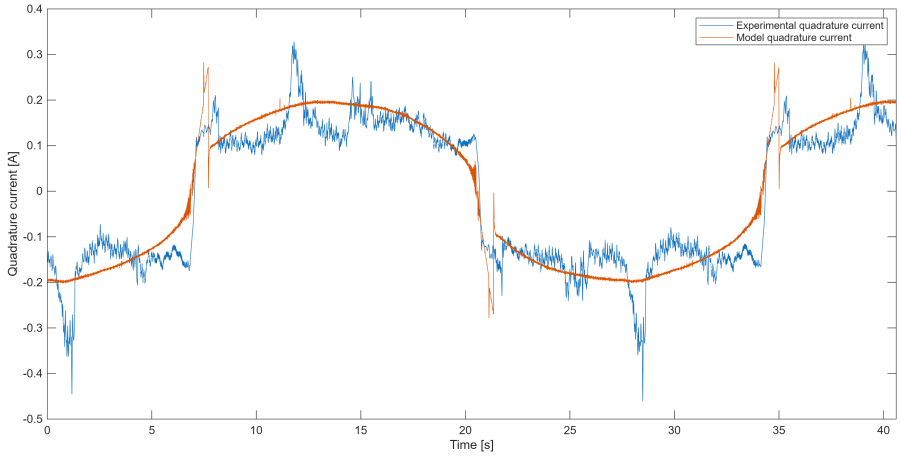

(c) Quadrature current

Figure 5.7: Experimental and simulated responses for Sample 3.

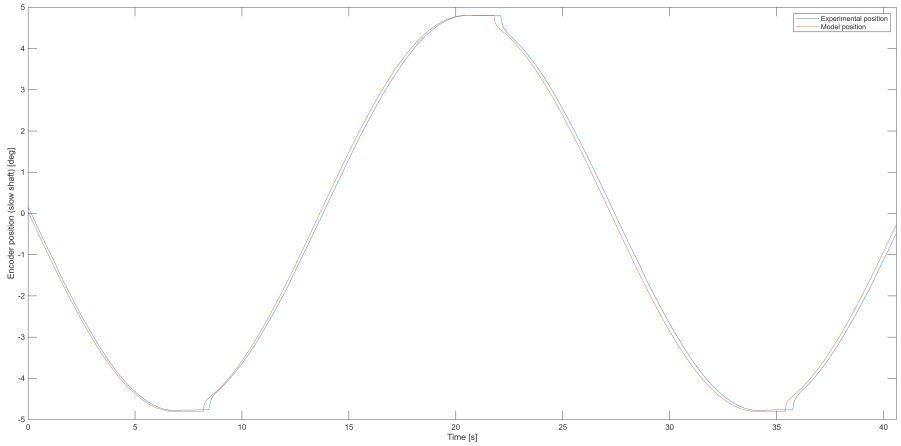

(a) Position

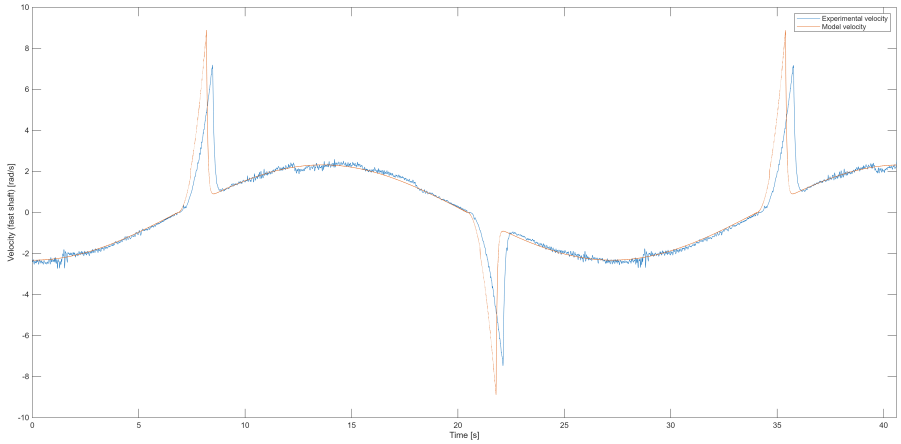

(b) Velocity

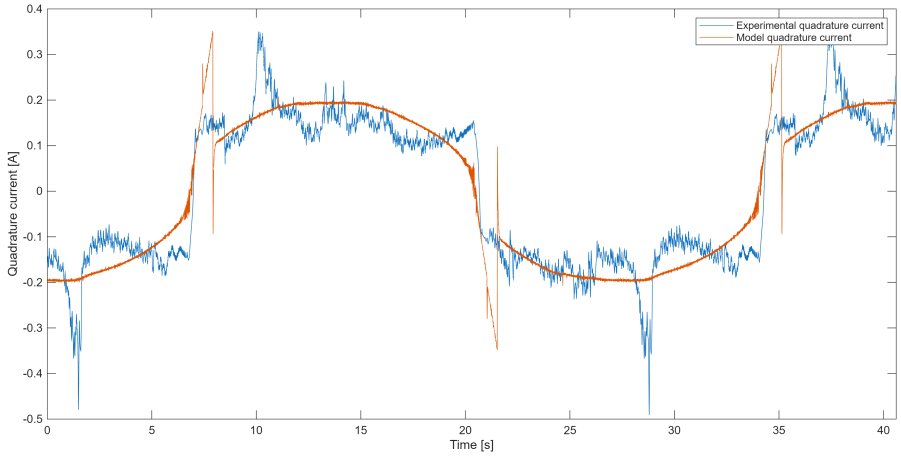

(c) Quadrature current

Figure 5.8: Experimental and simulated responses for Sample 5.

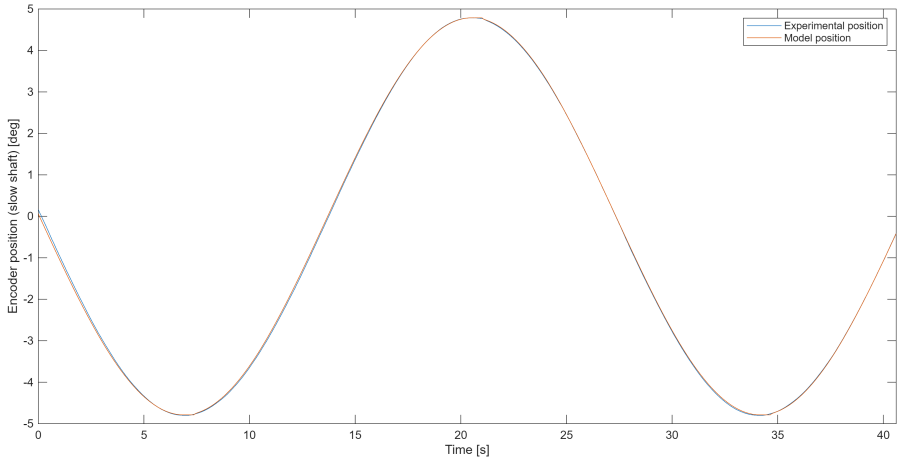

(a) Position

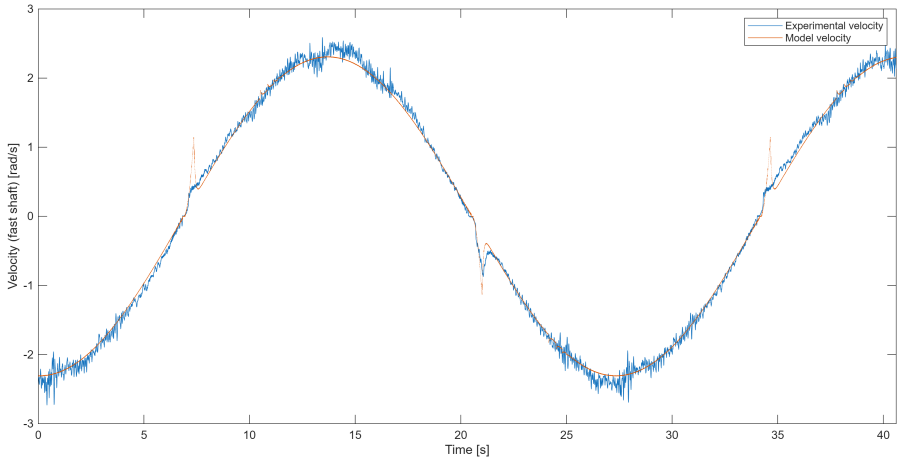

(b) Velocity

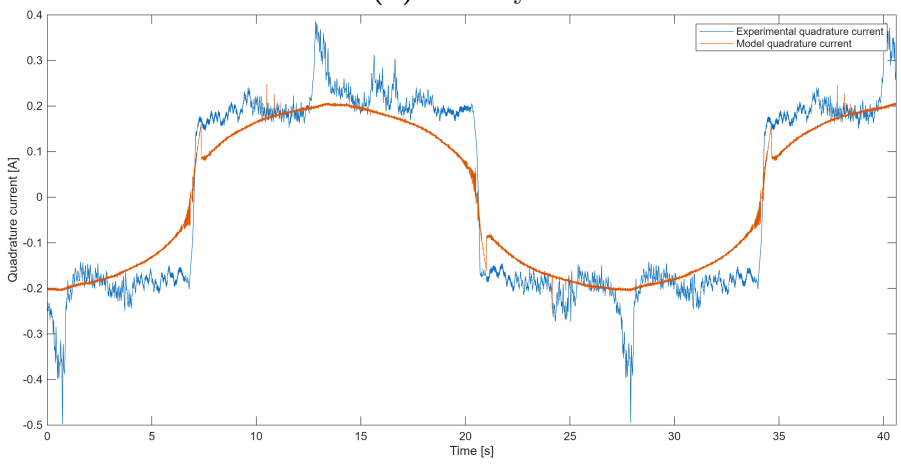

(c) Quadrature current

Figure 5.9: Experimental and simulated responses for Sample 6.

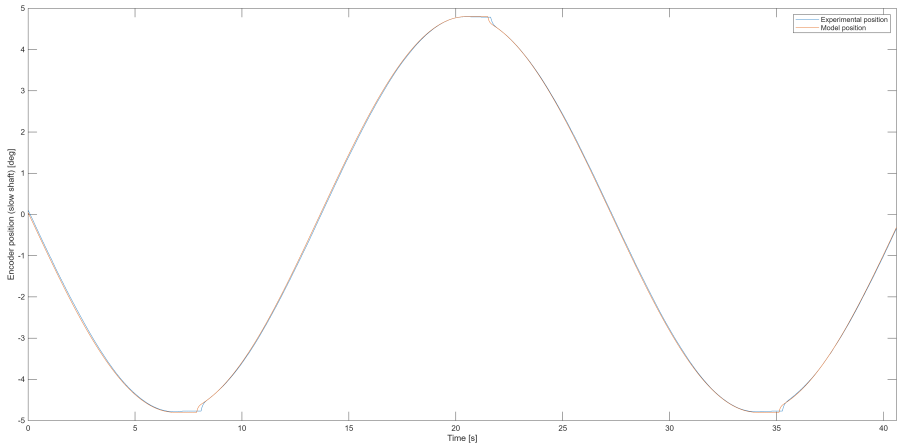

(a) Position

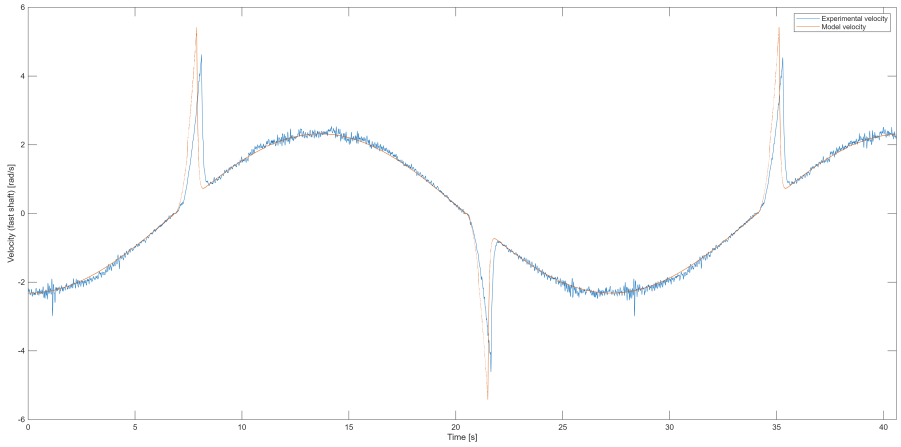

(b) Velocity

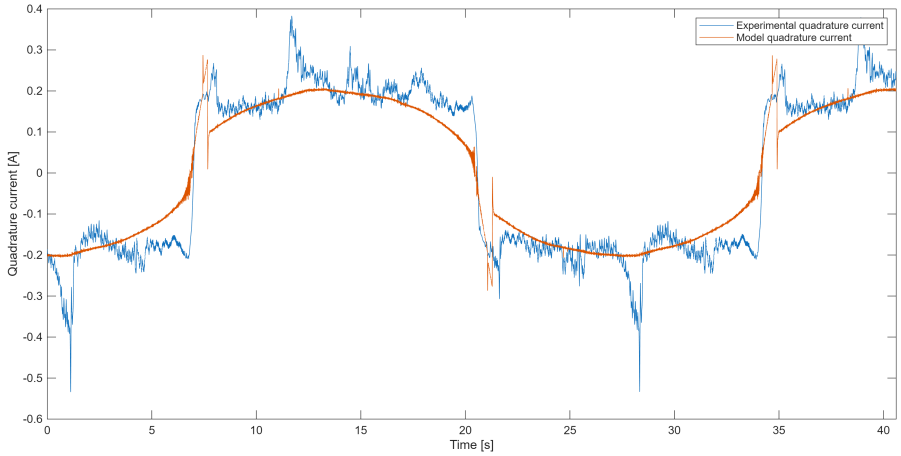

(c) Quadrature current

Figure 5.10: Experimental and simulated responses for Sample 8.

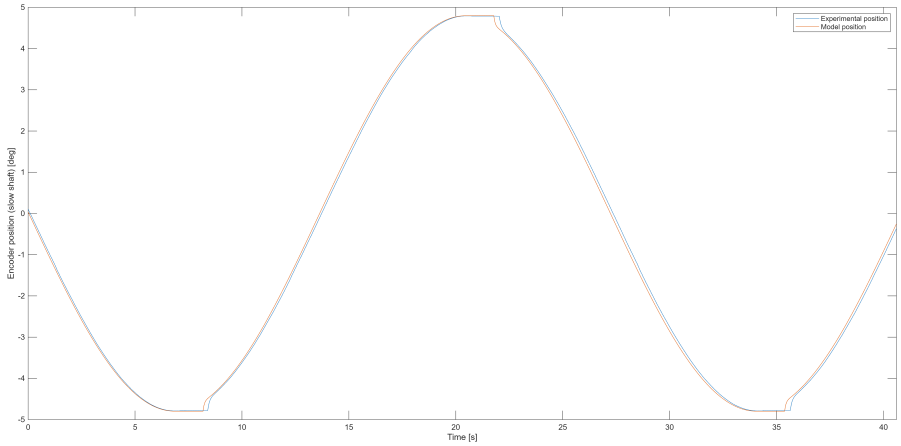

(a) Position

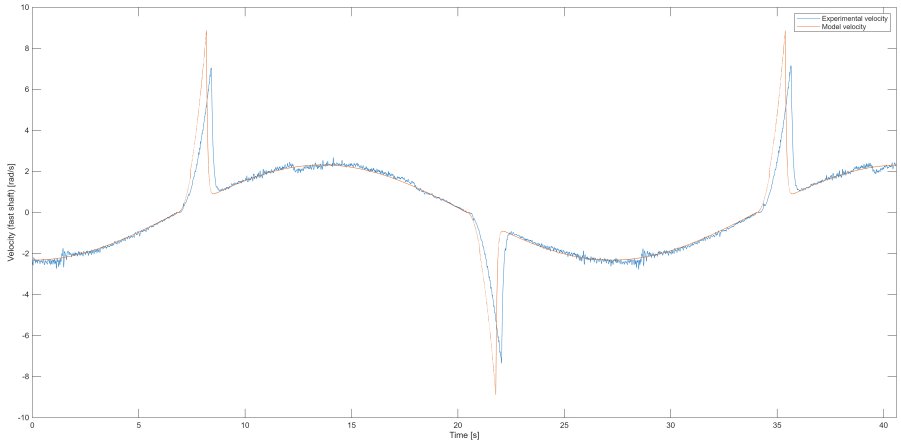

(b) Velocity

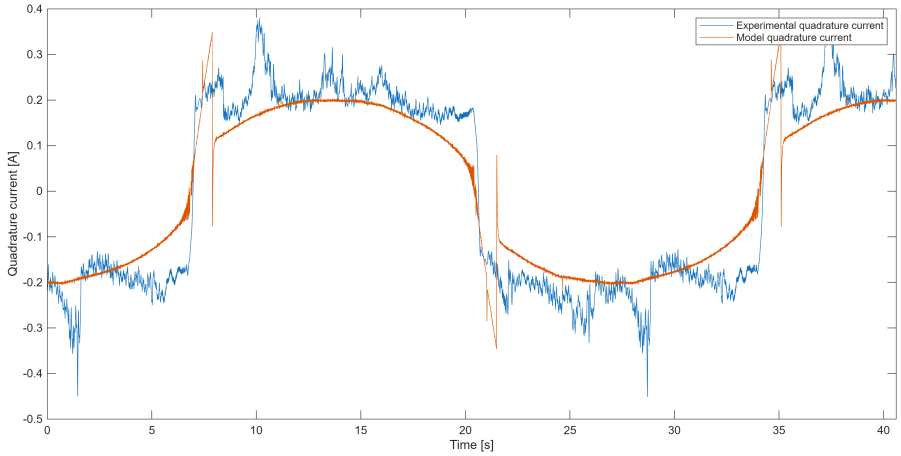

(c) Quadrature current

Figure 5.11: Experimental and simulated responses for Sample 10.

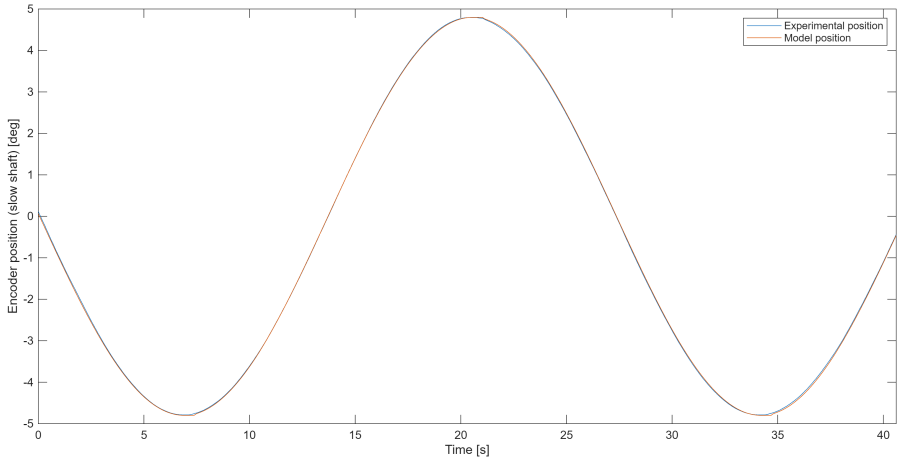

(a) Position

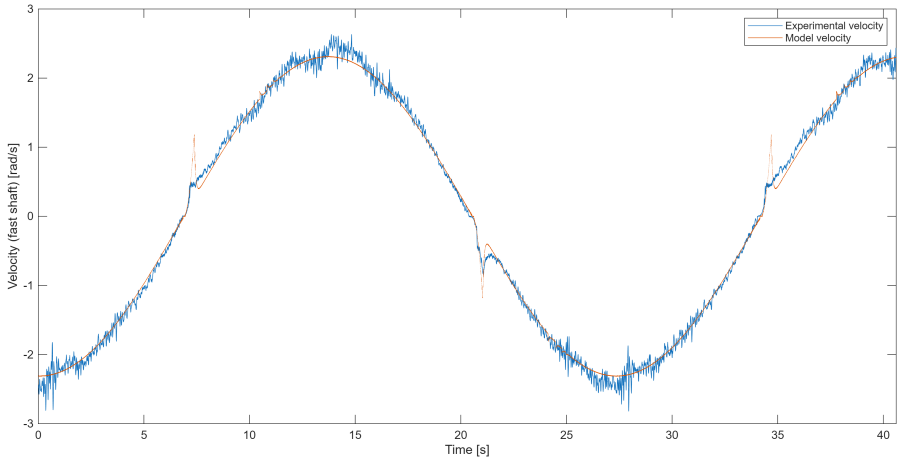

(b) Velocity

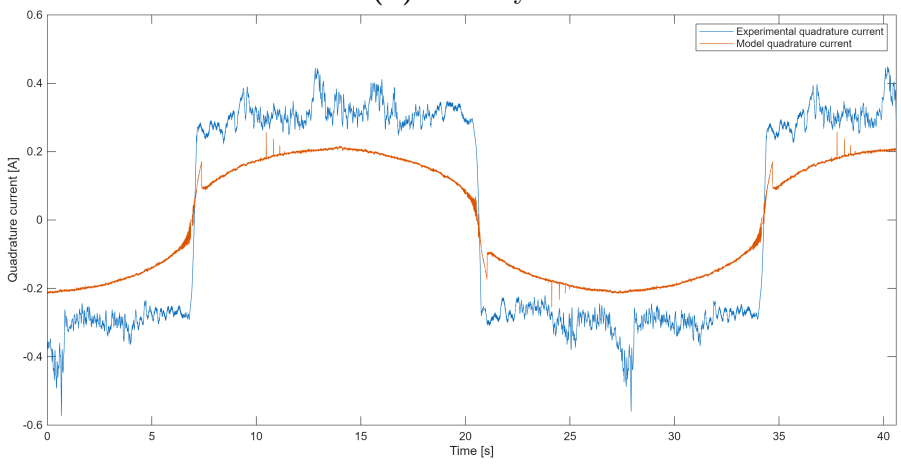

(c) Quadrature current

Figure 5.12: Experimental and simulated responses for Sample 11.

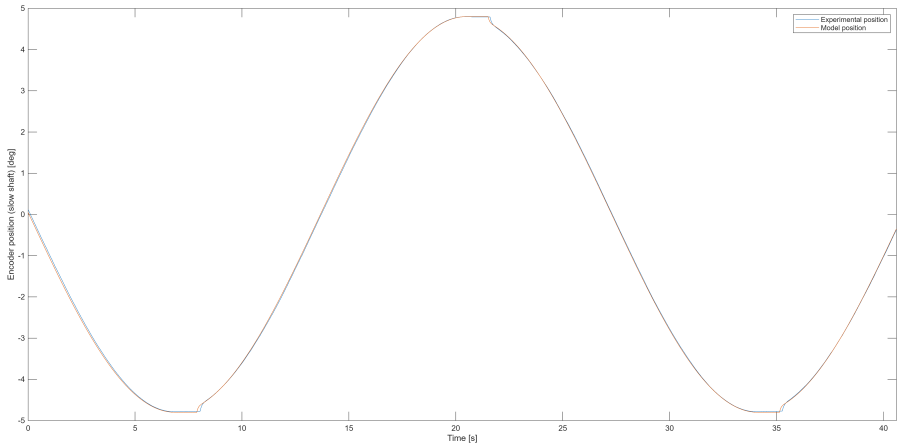

(a) Position

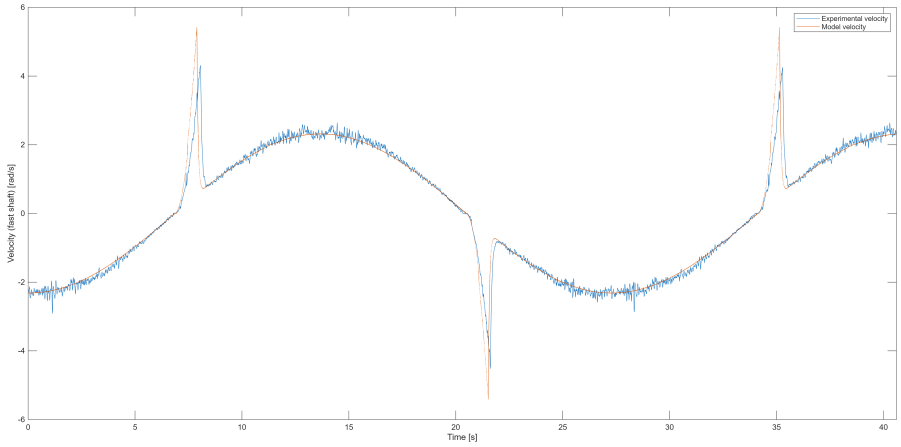

(b) Velocity

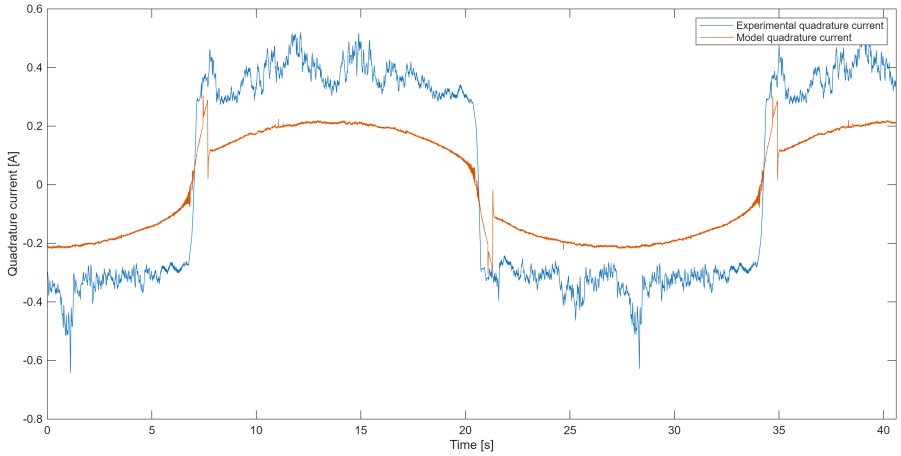

(c) Quadrature current

Figure 5.13: Experimental and simulated responses for Sample 13.

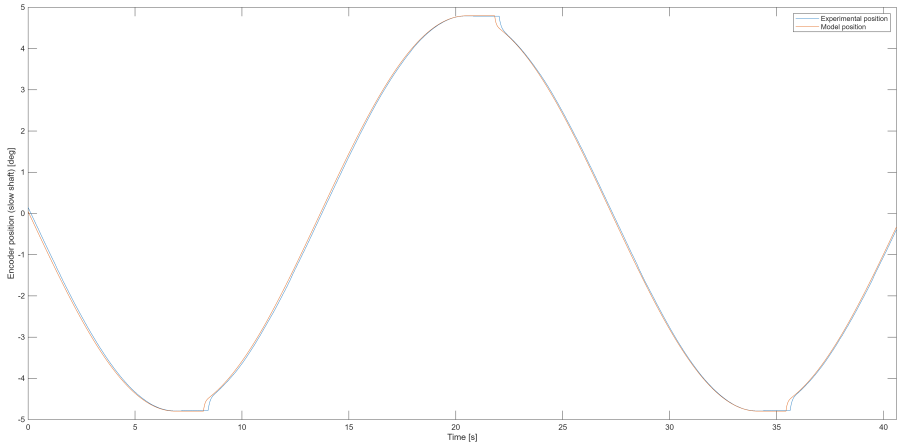

(a) Position

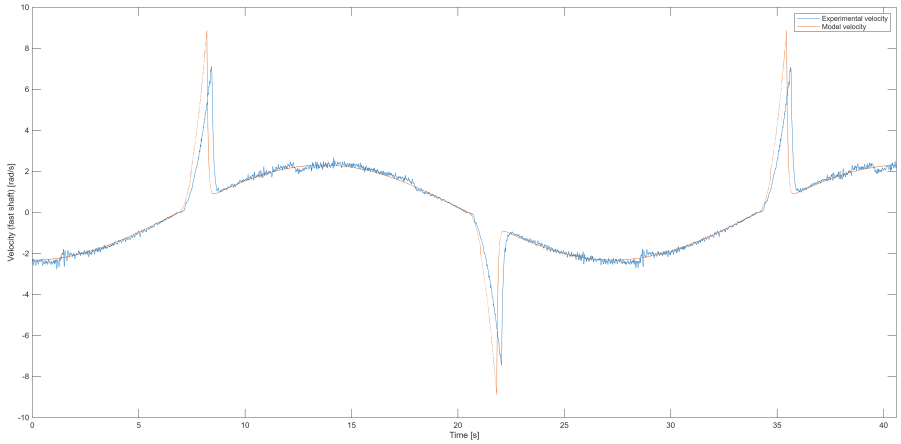

(b) Velocity

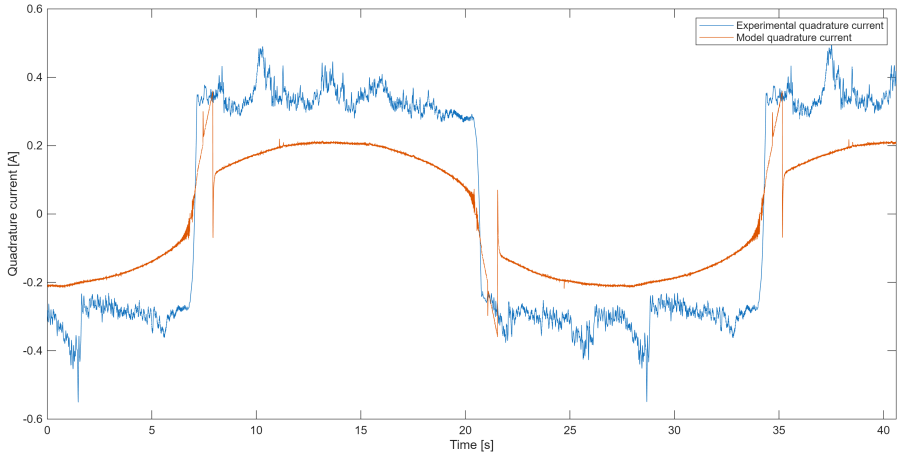

(c) Quadrature current

Figure 5.14: Experimental and simulated responses for Sample 15.

Chapter 6

Results analysis

In this chapter, a more in-depth analysis of the results presented in Chapter 5 is provided. First, the outcomes of the two mapping procedures are shown, together with the proposed polynomial fits for the acquired data. Second, a qualitative analysis of the comparison between the experimental results and the model outputs is carried out. This is followed by a quantitative assessment of the agreement between the two, based on the Root Mean Square Error (RMSE) computed for each test condition. Finally, an estimation of the simulation computing times is reported.

6.1 Load cell mapping

In this section, the Load Cell mapping results presented in Section 5.1, Table 5.1 are shown in Figure 6.1. As expected, the behaviour of the brake pad–disc interaction is nonlinear and exhibits saturation as the system approaches the non-contact condition. Considering this saturation and the slight periodic behaviour observed beyond it, a polynomial fit was performed with the objective of minimizing the $\text{NRMSE}_{\%}$ while keeping the polynomial order as low as possible. A rigorous definition of the RMSE and NRMSE can be found in Section 6.3.1. The selected polynomial $p_{lc}(x_1)$ as a function of the micro-mover 1 displacement is of fourth order and is reported below.

$$p_{lc}(x_1) = 0.06521x_1^4 - 0.1714x_1^3 + 0.1082x_1^2 - 0.4094x_1 + 0.7155$$

Quantity	**Value**
RMSE	0.0105
$\text{NRMSE}_{\%}$	1.48%

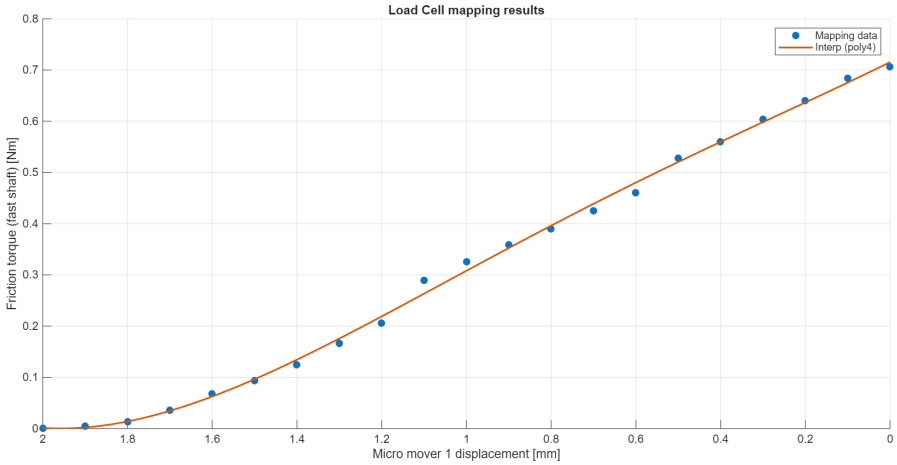

Figure 6.1: Load Cell mapping and polynomial fit

6.2 Gear backlash mapping

In analogy with the previous section, this part presents the results of the backlash mapping procedure described in Section 5.2, together with the corresponding theoretical predictions and a polynomial fit of the measured data. The experimental trend exhibits saturation at lower backlash values and an approximately linear behaviour for larger center distances between the two meshing gears. As done for the load-cell mapping procedure, Figure 6.2 shows the measured backlash data together with a polynomial fit obtained by seeking to minimise both the NRMSE and the polynomial degree. The selected third-order polynomial $p_{bk}(x_2)$, expressed as a function of the Micro-Mover 2 displacement, is reported below.

$$p_{bk}(x_2) = 0.001141x_2^3 - 0.0002408x_2^2 - 0.5448x_2 + 4.774$$

Quantity	**Value**
RMSE	0.0239
$\text{NRMSE}_{\%}$	1.47%

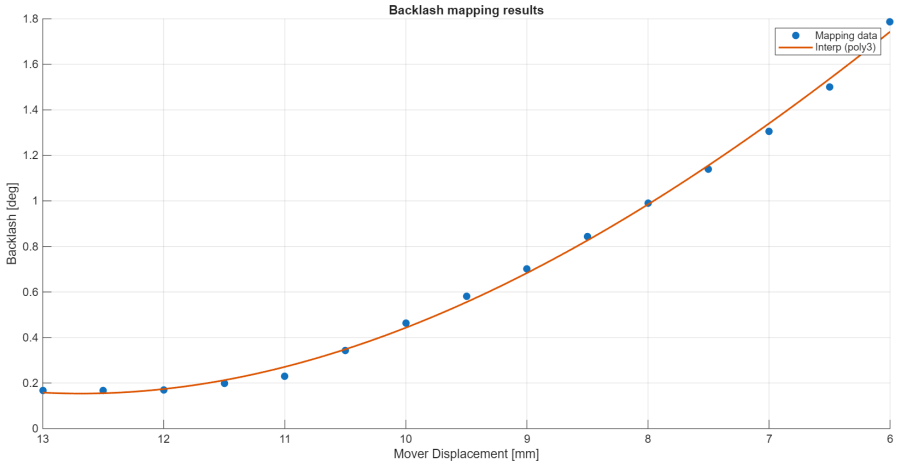

Figure 6.2: Backlash mapping and polynomial fit

Regarding the theoretical trend, as outlined in Section 4, the variation of normal backlash with respect to the change in center distance between the meshing gears is expected to be linear, with a slope equal to $2 \sin \alpha$, where α denotes the tooth pressure angle, taken as 20° for the gears considered:

$$\Delta j_n = 2\Delta a \sin \alpha$$

After a straightforward geometric derivation, the angular displacement can be expressed in terms of the center distance and the radius r of the selected gear , which for the reducer output gear is equal to 77.5 mm:

$$j_\theta = \frac{2a}{r} \tan \alpha$$

Figure 6.3 presents, on the same plot, the experimental backlash data together with the theoretical trend as functions of the center distance between the gears. The observed deviations from the theoretical behaviour consist primarily in the minimum backlash value achieved (which is zero in the theoretical prediction), in the nonlinear trend exhibited by the experimental data and in the markedly higher backlash values observed at larger center distances.
Nonetheless, an error analysis conducted between the theoretical prediction and the measured backlash data demonstrated that the resulting deviation lies within an acceptable range, as shown in Table 6.1.

A more detailed discussion of the origins of these deviations—primarily related to the impossibility, within the available time frame, of achieving through additive manufacturing the tight tolerances required for a near-theoretical involute meshing behaviour—is provided in the next section.

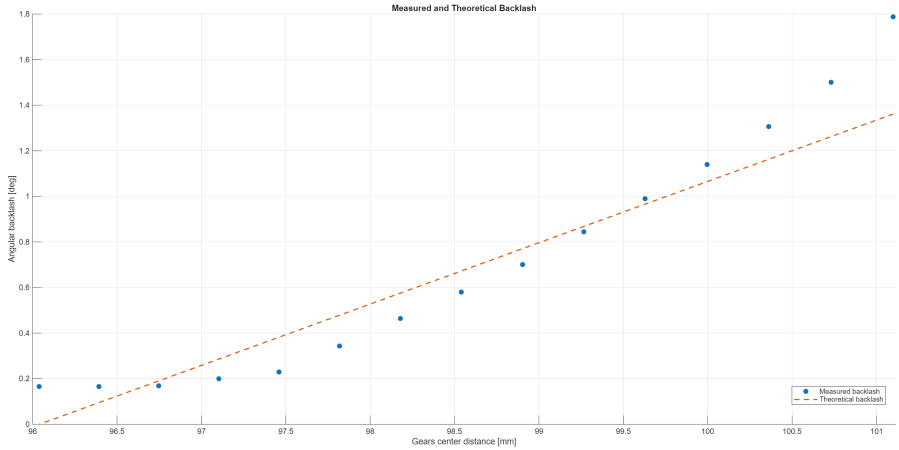

Figure 6.3: Measured and theoretical backlash trend

Quantity	Value
RMSE	0.6824
$NRMSE_{\%}$	11.59%

Table 6.1: Error between the theoretical and measured backlash trends

6.2.1 Impact of FDM Tolerances on Gear Meshing

In the analysis of low–gear-backlash conditions, it is essential to account for the geometric tolerances of the gears employed.
Tolerances in FDM-manufactured parts are strongly influenced by numerous process parameters, such as layer height, nozzle diameter, nozzle and bed temperatures, raster angle, and printing speed.[13]

Several experimental studies have shown that layer height is among the most influential factors affecting both surface accuracy and dimensional deviation. Specifically, variations in layer height have been reported to produce significant dimensional changes along all three principal directions, emerging as the most statistically influential parameter in ANOVA-based analyses [14].
Other investigations similarly indicate that planar dimensional precision is primarily governed by layer height and extrusion temperature [15].

Nozzle diameter has also been identified as an important contributor to planar resolution. Reducing the nozzle diameter from 0.6 mm to 0.2 mm has been shown to improve dimensional accuracy by approximately 5.1%, although this improvement comes at the cost of a substantial increase in total build time (around 53%) [16].

Finally, material shrinkage during FDM fabrication is widely recognized as a major source of dimensional deviation, with several works demonstrating its significant contribution to geometric inaccuracies in printed components [17].

In light of the considerations above, it follows naturally that a trade-off must be established between parameters that enhance part accuracy and those that favour overall printing speed. Such a trade-off was indeed implemented during the development of the test bench described in this study.
Since it was necessary to keep manufacturing times compatible with the timeframe of this thesis work—while also preserving sufficient margin to produce multiple versions of each component for optimisation purposes, and at the same time achieving tolerances adequate for the experimental activity—the following manufacturing parameters emerged as the outcome of this compromise:

Quantity	**Reduction drive gear**	**Encoder gear**
Nozzle diameter [mm]	0.4	0.25
Layer height [mm]	0.2	0.12
Printing time [-]	11h 41m	10h 48m
Estimated tolerance [mm]	0.18	0.11

Table 6.2: Gears FDM printing parameters

It should be noted that the tolerance values reported in Table 6.2 are not sourced from existing references; instead, they were derived using the following empirical rule adopted to ensure consistency in the design of the FDM-printed component, while limiting the dependence of dimensional accuracy on the wide set of known influencing parameters to a smaller subset of controllable variables—namely, layer height l_h and nozzle diameter d_n:

$$\text{tol} = 0.2\ l_h + \frac{n_d}{2}$$

6.3 Model results

In this section, an analysis of the model results presented in Section 5.3 is provided. The overall accuracy of the simulations, when compared with the experimental measurements, is generally satisfactory, particularly under near-nominal conditions (i.e., low backlash and low friction).

The model results able to accurately reproduce the behaviour of the external encoder position, including the presence of backlash and friction effects when present. While the transition into the backlash region occurs almost simultaneously with the experimental data, the transition out of this region shows a slight delay. This discrepancy becomes more evident for larger backlash values and is likely related to the way the backlash phenomenon is modeled. As introduced in Chapter 3, backlash is represented using a built-in Simulink block that introduces a simple dead-band on the signal. Although this approach proves sufficiently accurate for small backlash values, it becomes inadequate for larger values, as it cannot fully capture the underlying physical complexity of the gear meshing process—such as tooth elastic deformations or gear inertia.
The delay observed is sufficiently small ($< 0.25s$) relative to the characteristic time scales of the dynamics under consideration. Its mitigation, which would require a more comprehensive modelling of the backlash phenomenon and its interaction with dry friction, is therefore considered beyond the scope of this work.

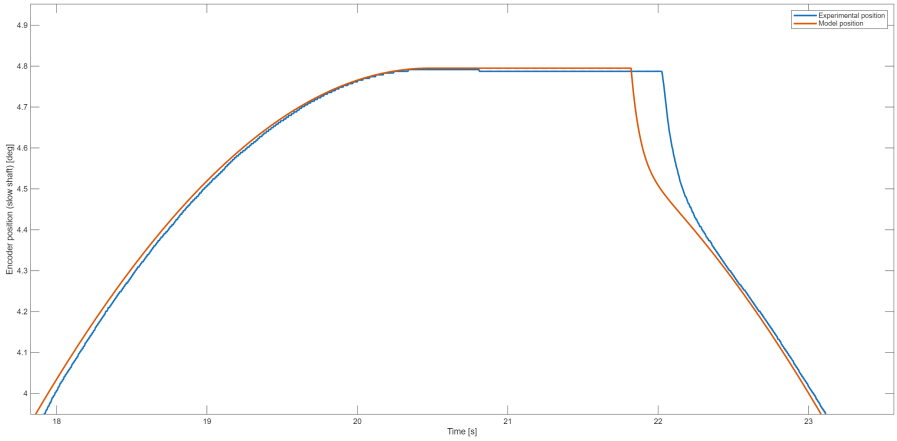

Figure 6.4: High backlash behavior- model and measured position

As for the velocity profiles, the model manages to closely represent the measured behaviour, producing a signal that mostly matches a filtered representation of the experimental data. The characteristic velocity spikes of a backlash-affected closed-loop system are also correctly reproduced, with a sufficiently low latency ($<$ 0.3 s).

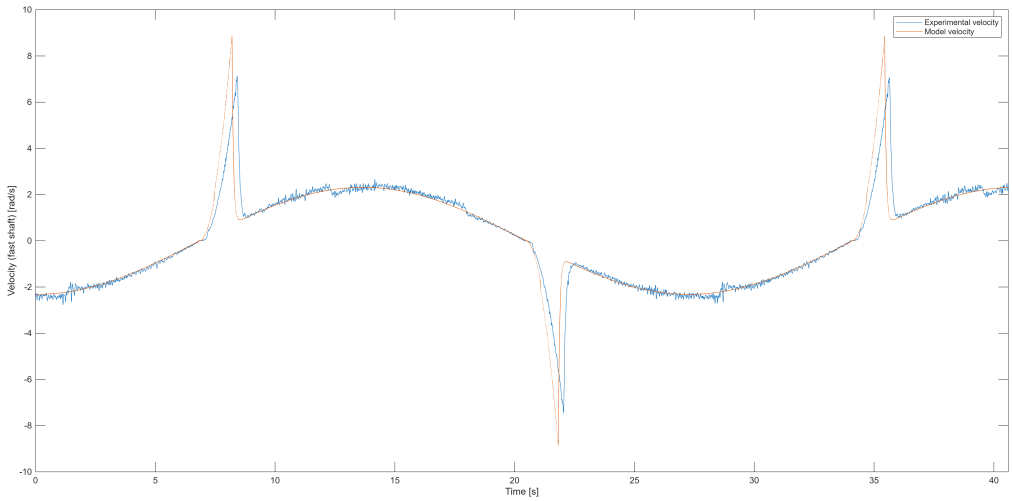

Figure 6.5: High backlash - high friction behavior- model and measured velocity

Finally, regarding the simulated quadrature current, the overall behaviour appears satisfactory in terms of synchronicity with the measured currents across all test conditions. In general, backlash does not seem to affect the model's ability to reconstruct the actual mean current value, and the controller-induced spikes observed at high-backlash settings are also correctly reproduced.
A less accurate behaviour, however, is observed at high friction-torque values. In these cases, the simulated current is lower than the average measured quadrature current, with discrepancies reaching up to a relative error of approximately 43% in the worst case. The origin of this mismatch is believed to lie in the parametrization of the electrical subsystem within the model.
When the original model parameters were tuned, most electrical and control parameters were identified through an optimization process aimed at fitting the measurements from the previous version of the test bench. Since carrying out an optimization process of comparable scale was considered beyond the scope of this work, the level of accuracy achieved was deemed adequate for the preliminary nature of the model-response assessment.

6.3.1 Position error analysis

In this section, the error between the measured and simulated positions is analysed. This is quantified through the computation of the Normalized Root Mean Square Error (NRMSE), where the simulated position signal is treated as the observed value and the encoder position measured on the test bench is considered as the predicted value.

The NRMSE between the observed values y_i and the predicted values $\hat{y}_i$ is defined as follows:

$$NRMSE \triangleq \frac{RMSE}{\hat{y}_{\max} - \hat{y}_{\min}}$$

$$RMSE \triangleq \sqrt{\sum_{i=1}^{n} \frac{(\hat{y}_i - y_i)^2}{n}}$$

and is expressed as a percentage to facilitate interpretation in the heat map shown in Figure 6.6.

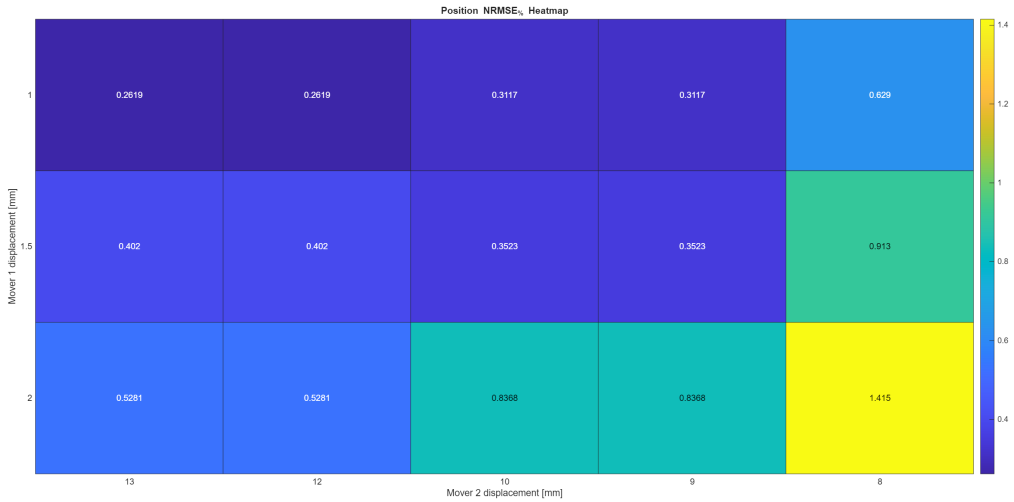

Figure 6.6: Position $\text{NRMSE}_{\%}$ heatmap

As shown in Figure 6.6, the highest values of $NRMSE_{\%}$ occur under conditions of low friction and high backlash. This behaviour is primarily attributed to the mechanisms discussed at the beginning of this Section —namely, the influence of large backlash on the simulated position. The effect is most pronounced at low friction levels, since higher friction tends to couple the two modelled phenomena more strongly, thereby reducing the visible impact of backlash-related discrepancies.

6.3.2 Velocity error analysis

In analogy with the previous section, Figure 6.7 shows the heat map of the percentage NRMSE between the simulated and measured velocity signals. The first aspect to note is that the error is nearly independent of the friction condition. This behaviour is consistent with the nature of dry friction, as velocity and dry friction are essentially independent phenomena that do not directly influence one another.

A second observation concerns the increase in error at higher values of gear backlash. As previously discussed, the presence of backlash in the position feedback loop causes the controller to generate sudden current spikes when the system enters or leaves the dead band, which in turn produces sharp velocity variations at the corresponding instants.
Under these critical conditions, discrepancies between simulated and actual velocity tend to accumulate, since the control logic implemented in the model does not perfectly match that of the real controller.

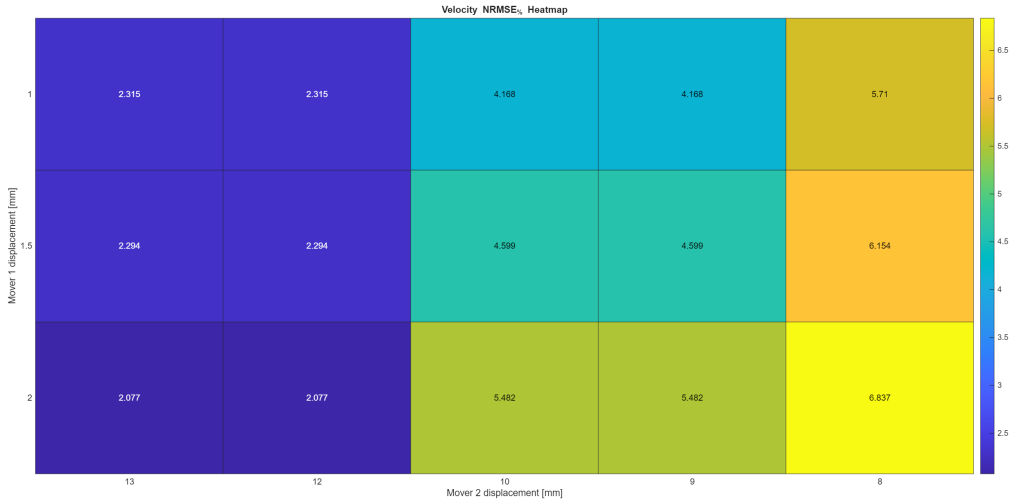

Figure 6.7: Velocity $\text{NRMSE}_{\%}$ heatmap

Overall, the NRMSE values obtained for the velocity are noticeably higher than those calculated for the position. This outcome is, however, fully consistent with the expectations expectations of this work. The mechanisms leading to these deviations have been clearly identified and are well understood within the framework of the present analysis.
In light of these considerations, the accuracy achieved at this stage is regarded as satisfactory and adequate for the current phase of model development, while also providing a solid basis for future refinement and extension of the simulation framework.

6.4 Computing times

The computational performance of the simulation model was evaluated by analysing the execution time associated with each test case. Since the selected integration method (Euler 1) employs a fixed integration step, the computing time is directly determined by the total number of integration steps. For each simulation, the elapsed time was recorded together with the corresponding time vector, from which both the physical duration and the total number of solver steps were obtained.

To enable a meaningful comparison between simulations of different lengths, the computational cost was expressed by normalizing the elapsed time by the simulated time interval, yielding a metric in units of:

$$\texttt{cost} = \frac{\texttt{computation time [s]}}{\texttt{time of simulated dynamics [s]}}$$

This indicator allows assessing the computational cost of the model independently of the simulation duration.

The results show an almost constant computational cost per simulated second averaging 8.48 s across all the 15 test points, with a standard deviation of 2.09. This confirms that the model scales linearly with the number of integration steps—a behaviour fully consistent with the use of a fixed-step solver. Minor deviations were observed in a limited subset of test cases, which can be attributed to transient phenomena and local increases in model stiffness.
The resulting trends demonstrate that the model maintains an almost constant computational cost per simulated second, confirming its suitability for large-scale batch simulations and wide parametric analyses.

Chapter 7

Conclusions and future developments

This final chapter summarises the main outcomes of the work carried out in this thesis and reflects on the insights gained throughout the experimental and modelling activities. The preceding chapters have described the design modifications implemented on the EMA test bench, the experimental campaigns performed to characterise key nonlinear phenomena, and the subsequent validation of the high-fidelity simulation model. Here, a concise yet comprehensive overview of the results is provided, highlighting the effectiveness of the adopted solutions and the extent to which the objectives of the thesis have been achieved, followed by a brief discussion of the main themes identified as potential subjects for future work.

7.1 Conclusions

The work presented in this thesis has focused on the redesign, refinement, and experimental characterization of an Electromechanical Actuator (EMA) test bench, together with the validation of an existing high-fidelity simulation model.
The modifications introduced on the experimental setup, the methodologies implemented, and the comparative analysis between simulated and measured data have provided significant insight into the nonlinear behaviours that typically arise in aerospace actuation systems—most notably gear backlash and dry friction.

First, the applied design modifications to the test bench have proven to be both functional and well integrated. The newly implemented elements—including the redesigned gearbox assembly, the backlash-regulating interface, and the improved friction-generation module—have demonstrated reliable performance throughout

the experimental campaign. These enhancements not only ensure the correct operation of the apparatus, but also significantly increase confidence in the observation and quantification of the studied nonlinearities.
As a result, the updated bench now represents a much more controlled and reproducible environment for analysing phenomena such as stick–slip, hysteresis, backlash, and the interaction between these effects.

A further important achievement relates to the mapping of the two micro-movers, respectively responsible for regulating backlash and friction torque. Both mapping procedures yielded highly repeatable trends, which were successfully interpolated with polynomial functions showing a good level of confidence. This indicates that—provided that a rigorous calibration procedure is carried out before each experimental session—the measured displacements can be reliably used to reproduce the desired backlash or friction values.

Second, the FDM-manufactured motor shaft, introduced to reduce manufacturing complexity, costs, and production time during this thesis work, yielded performance results that can be considered satisfactory—particularly with respect to torsional stiffness. The current configuration employs a 70% printing infill, which has ensured adequate rigidity for the characterization tasks carried out.
Nevertheless, the possibility of producing shafts with lower infill percentages remains an interesting direction for future research. Such variations would enable a systematic exploration of the effects of reduced torsional stiffness on closed-loop position-control performance, while also opening opportunities to investigate how these additional flexibilities could be parametrized and incorporated into the simulation model.

Third, the redesigned friction-generation system has proven markedly more representative of a true friction phenomenon compared with the legacy PI-controlled servomotor. The previous configuration behaved more like an opposing load rather than an actual friction torque acting directly on the actuation line, and it was strongly influenced by the interaction of multiple overlapping control loops.
By replacing it with a mechanically driven, displacement-controlled braking mechanism, these critical dependencies were eliminated. The resulting friction generation is now physically more coherent, easier to modulate, and better suited for experimental reproduction of stick–slip and other dry-friction effects, while avoiding instabilities related to coupled feedback dynamics.

Finally, the simulation model demonstrated a strong capability to capture and reproduce off-nominal operating conditions. The comparison between measured and simulated variables shows a high level of coherence, particularly in terms of position tracking. In many of the analysed cases, the normalized position error remained below 0.5%, and even in the most severe off-nominal scenarios the position

error never exceeded 1.5%.
These results confirm both the validity of the modelling approach and its suitability for future prognostic applications. However, it must also be acknowledged that the accuracy achieved in position reproduction is not fully matched in the velocity and quadrature-current domains. Discrepancies observed in these quantities suggest that the electrical and control parameters—originally optimised using data from an older version of the bench—are no longer fully representative of the updated system.
A comprehensive re-identification and optimisation of the model parameters is therefore necessary to further improve simulation fidelity, especially for variables directly influenced by the electromagnetic and current-control subsystems.

In conclusion, the updated EMA test bench, combined with the validated simulation framework, constitutes a robust platform for the study of nonlinear actuator behaviour and lays the foundation for future advancements in model-based prognostics and health-monitoring strategies. The work carried out in this thesis not only improves the experimental capabilities of the bench but also deepens the understanding of the complex interactions that govern the behaviour of electromechanical actuators under realistic operating conditions, opening new scenarios for refinement and future research.

7.2 Future Developments

Building on the results achieved in this work, several directions for future development can be identified. These improvements would enhance both the flexibility of the experimental bench and the predictive capabilities of the simulation model.

As outlined in the previous section, a first and highly accessible extension concerns the study of the effects of reduced torsional stiffness in the motor shaft. Given that the shaft is fabricated through low-cost FDM additive manufacturing, exploring variants with different infill percentages, printing materials, or internal geometries would be straightforward. Such modifications would allow the creation of a family of interchangeable shafts with tailored torsional properties, enabling the construction of an adaptable transmission line capable of more closely reproducing the behaviour of the reference actuation system.
The influence of reduced stiffness could be investigated both experimentally—by observing its effects on position control, velocity regulation, and dynamic response—and in simulation, by appropriately modifying the mechanical parameters of the model.
A similar approach could be applied to the custom elastic joint designed in this

work. Since its optimal geometry has already been developed and validated, producing variants with different stiffness or damping characteristics would allow an experimental modulation of viscous effects in the transmission and further enrich the bench configurability.

Another recommended development direction concerns the electrical modelling of the three-phase synchronous motor. The current implementation has the advantage of being highly versatile and capable of representing a wide range of motor types with acceptable accuracy. However, when applied to the specific motor under study, its predictive performance is limited by the simplified representation of more complex electromagnetic phenomena—such as the behaviour of distributed windings or magnetic saturation effects. A future refinement of the electromagnetic submodel, possibly integrating more detailed physical descriptions or parameter estimation, would significantly enhance the accuracy of current and torque predictions and reduce some of the discrepancies highlighted in Chapter 6.

As discussed in Chapter 6, a large portion of the differences between measured and simulated backlash behaviours originates from the simplified modelling approach based on the built-in Simulink backlash block. While sufficiently accurate in near-nominal conditions, this block is inherently unable to fully capture secondary effects such as gear inertia during motion reversals and elastic deformation of the gear teeth.
A more detailed backlash model—potentially involving multi-body dynamics or a refined representation of involute tooth geometry—would improve the ability of the simulation to replicate real behaviour across a broader range of conditions.

Finally, although the model shows very good accuracy in terms of position tracking, many of its parameters are still based on a previous optimisation procedure performed on an earlier configuration of the bench. These include control-related parameters (e.g., PID gains), mechanical quantities (viscous damping, inertia), and electrical parameters. A dedicated re-tuning campaign, possibly leveraging modern optimization techniques based on parameter estimation, is expected to improve the accuracy of velocity and quadrature current predictions, which currently exhibit larger discrepancies under high-friction or high-backlash conditions.

Bibliography

[1] Mohammed Echarif Aguida, Yanbo Che, and Jianxiong Yang. «Technological advancements and future prospects of electrical power systems for sustainable more electric aircraft». In: *Propulsion and Power Research* 13.4 (2024), pp. 475–486. ISSN: 2212-540X (cit. on p. 2).

[2] A. J. Forsyth A. A. AbdElhafez. «A Review of More-Electric Aircraft». In: (2009) (cit. on p. 2).

[3] Paolo Maggiore and Matteo D.L Dalla Vedova. «Modellazione, simulazione e sperimentazione dei sistemi aerospaziali». In: *Azionamenti elettrici - University lecture*. Politecnico di Torino, 2024 (cit. on pp. 2, 5).

[4] Gaetano Quattrocchi, Alessandro Iacono, Pier C. Berri, Matteo D. L. Dalla Vedova, and Paolo Maggiore. «A New Method for Friction Estimation in EMA Transmissions». In: *Actuators* 10.8 (2021). ISSN: 2076-0825 (cit. on p. 3).

[5] F. Lewis et al G. Vachtsevanos. «Fault Prognosis». In: *Intelligent Fault Diagnosis and Prognosis for Engineering Systems*. John Wiley & Sons, Ltd, 2006. Chap. 6, pp. 284–354 (cit. on p. 3).

[6] Jianhui Luo, Madhavi Namburu, Krishna Pattipati, Liu Qiao, Masayuki Kawamoto, and SACS Chigusa. «Model-based prognostic techniques [maintenance applications]». In: *Proceedings AUTOTESTCON 2003. IEEE Systems Readiness Technology Conference.* Ieee. 2003, pp. 330–340 (cit. on p. 4).

[7] Adhavan Balashanmugham and Mockaisamy Maheswaran. «Permanent-Magnet Synchronous Machine Drives». In: *Applied Electromechanical Devices and Machines for Electric Mobility Solutions*. IntechOpen, 2019. Chap. 2 (cit. on p. 7).

[8] Paolo Mercorelli. «Identification of Parameters and States in PMSMs». In: *Electronics* 12.12 (2023). ISSN: 2079-9292 (cit. on p. 7).

[9] George Vachtsevanos Kai Goebel and Marcos E. Orchard. «Prognostics». In: 2013 (cit. on p. 8).

[10] Brian Armstrong-Hélouvry, Pierre Dupont, and Carlos Canudas De Wit. «A survey of models, analysis tools and compensation methods for the control of machines with friction». In: *Automatica* 30.7 (1994), pp. 1083–1138. ISSN: 0005-1098 (cit. on p. 9).

[11] Paolo Maggiore and Matteo D.L Dalla Vedova. «Modellazione, simulazione e sperimentazione dei sistemi aerospaziali». In: *Friction Models - University lecture*. Politecnico di Torino, 2024 (cit. on pp. 9–12).

[12] Mohammad Hossein Same, Gabriel Gandubert, Gabriel Gleeton, Preslav Ivanov, and René Landry. «Simplified Welch Algorithm for Spectrum Monitoring». In: *Applied Sciences* 11.1 (2021). ISSN: 2076-3417. DOI: 10.3390/app11010086. URL: https://www.mdpi.com/2076-3417/11/1/86 (cit. on p. 48).

[13] Azhar Equbal, Ramesh Murmu, Veenit Kumar, and Md. Asif Equbal. «A recent review on advancements in dimensional accuracy in fused deposition modeling (FDM) 3D printing». In: *AIMS Materials Science* 11.5 (2024), pp. 950–990. ISSN: 2372-0484. DOI: 10.3934/matersci.2024046. URL: https://www.aimspress.com/article/doi/10.3934/matersci.2024046 (cit. on p. 67).

[14] Muhammad Abas, Tufail Habib, Sahar Noor, Bashir Salah, and Dominik Zimon. «Parametric Investigation and Optimization to Study the Effect of Process Parameters on the Dimensional Deviation of Fused Deposition Modeling of 3D Printed Parts». In: *Polymers* 14.17 (2022). ISSN: 2073-4360. DOI: 10.3390/polym14173667. URL: https://www.mdpi.com/2073-4360/14/17/3667 (cit. on p. 67).

[15] Irene Buj-Corral, Ali Bagheri, and Maurici Sivatte-Adroer. «Effect of Printing Parameters on Dimensional Error, Surface Roughness and Porosity of FFF Printed Parts with Grid Structure». In: *Polymers* 13.8 (2021). ISSN: 2073-4360. DOI: 10.3390/polym13081213. URL: https://www.mdpi.com/2073-4360/13/8/1213 (cit. on p. 67).

[16] Mr.G.Dhayanithi, Bala Surya M, Mohanbabu K, Mohamed Naveeth N, Sri Sakthivel P, and Sethubathi Jagadeesan. «Investigating the Effects of Nozzle Diameter Variation on Additive Manufacturing Process». In: *International Journal of Innovative Research in Technology* 11.5 (Oct. 2024), pp. 1732–1734. ISSN: 2349-6002 (cit. on p. 67).

[17] Anoop K. Sood, Raj K. Ohdar, and Siba S. Mahapatra. «Experimental investigation and empirical modelling of FDM process for compressive strength improvement». In: *Journal of Advanced Research* 3.1 (2012), pp. 81–90. ISSN: 2090-1232. DOI: https://doi.org/10.1016/j.jare.2011.05.001 (cit. on p. 68).